

Poster/demo slide deck

Monday 8 - Fireslide Session

Poster & Demonstration Session

When: Thursday after the zoom session ends

Where: in [gather.town](#) in the poster & demo rooms

What: 19 posters

4 demos (note times)

Details on the conference website [poster/demo page](#)

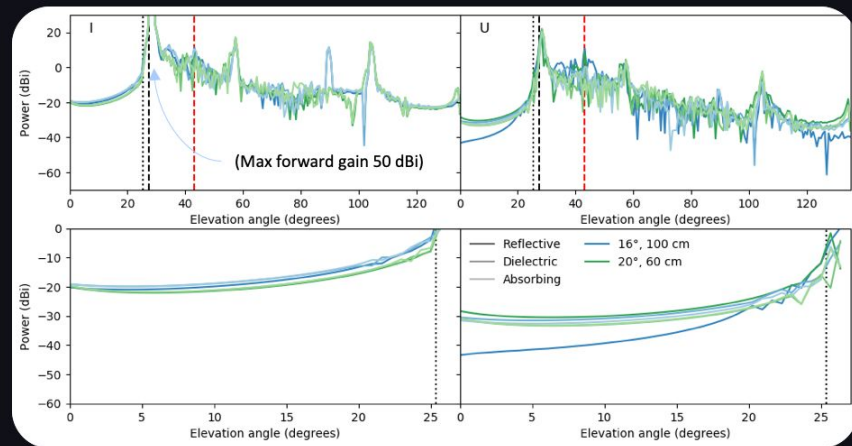
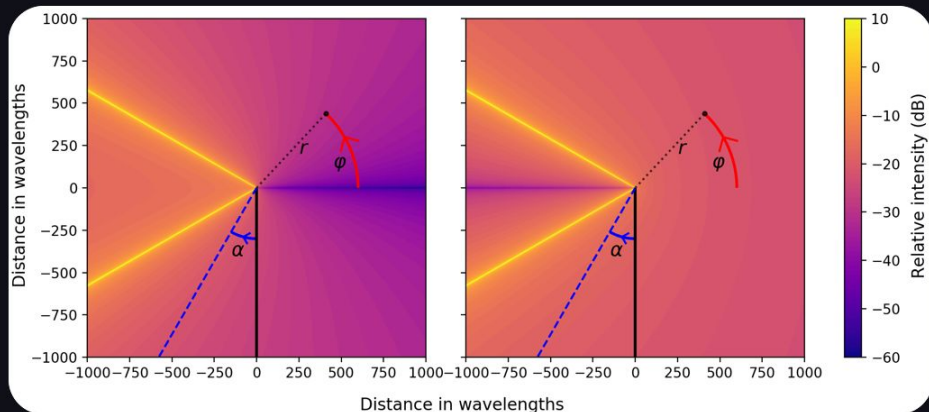


POSTERS

Modeling sidelobes with GTD

Alexandre Adler, Jón Gudmundsson, Proc. SPIE 11453, [arxiv:2012.07613](https://arxiv.org/abs/2012.07613)

- Full Physical Optics simulation of Small Aperture Telescopes (including ground screen) is computationally intensive.
- GTD extends GO, includes rules for diffraction of rays on edges.
- Modelling using GRASP.
- Studied: Forebaffle length, material properties, flare radius, off-center pixels.



Machine Learning Simulations of the Microwave Sky

Dongwon 'DW' Han, Neelima Sehgal et al.



(1) Summary

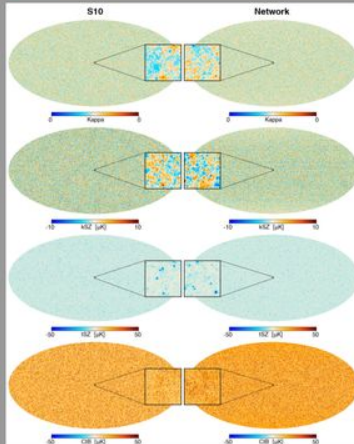
Current and future high-resolution CMB experiments, such as ACT, SPT, SO, CMB-S4 and CMB-HD will observe large sky areas at arcminute resolution or better with unprecedented sensitivity.

CMB data analyses rely on simulations for many different tasks (e.g. to generate covariance matrices used in likelihood analyses and investigate biases.)

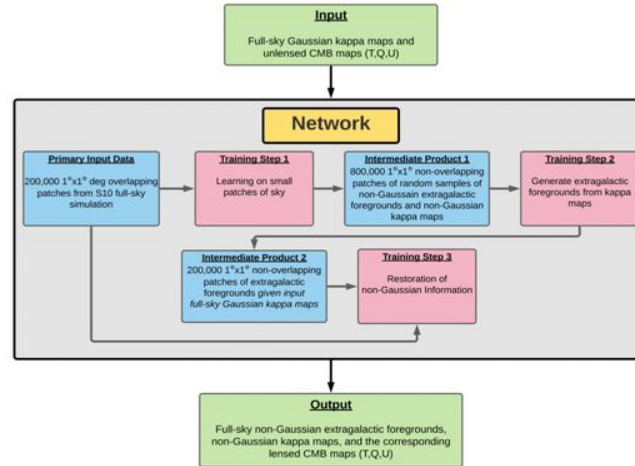
There are a few full-sky extragalactic simulations available that include non-Gaussian information and correlated foregrounds [e.g. S10 model (Sehgal et al, 2010), WebSky (Stein et al, 2020)]. However, they have a limited number of independent realizations.

In this work, we use generative machine learning models to generate **500 full-sky realizations** of the S10 full-sky simulations. We will make these 500 realizations public as soon as the paper is released.

(3) Results



(2) Method



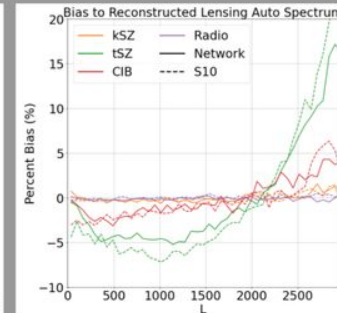
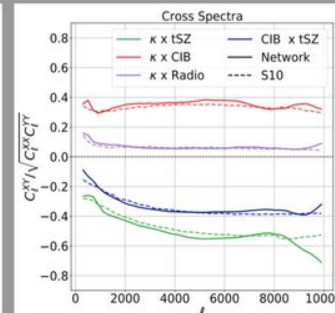
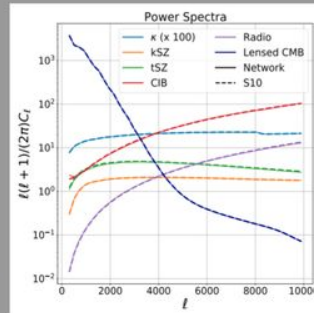
(4) Conclusions

In this study, we find that machine learning techniques can be used to reproduce the statistics of existing simulations that include non-Gaussian information and correlations. Furthermore, this can be done with much lower computational cost than rerunning the full N-body simulation pipelines.

The **potential application** of these simulations include

- (1) replacing Gaussian foreground simulations throughout CMB data analysis to generate realistic covariance matrices and to accurately capture foreground biases
- (2) using the network as a part of forward-modeling, taking advantage of lower computational cost.

We plan to make these 500 simulation realizations available via LAMBDA and NERSC in both CAR and HEALPIX format, for six frequencies at 0.5 arcmin resolution. The lensed CMB maps have both temperature and polarization.



Beam Side lobe Convolutions

1. Performed Simulations with available GRASP optical simulations
 - 4pi Beam
 - Far Side Lobes
 - Near side lobes (10% bias)
 - Main lobes
2. Inputs:
 - Galaxy (PySM)
 - Radio sources (PS4C)
 - No instrumental noise
3. Runs on 183 NERSC-KNL nodes :
 - For all LiteBIRD frequency channels
 - partially populated focal planes (see Table 1)

LFT	MFT	HFT
12	39	13
24	52	13
24		13
24		

Table 1. Number of pixels accounted for TOAST simulations (color scheme follows LB freq. bands).

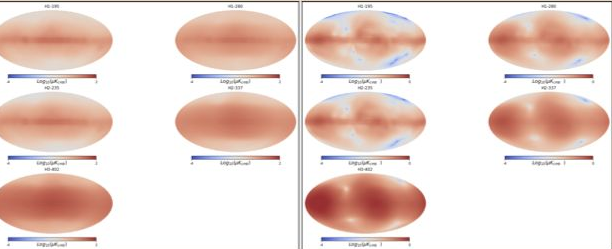


Figure1. Far side lobes (>20 deg) for a subset of High frequency channels, for (left) Unpolarized and (right) Polarized intensity maps.

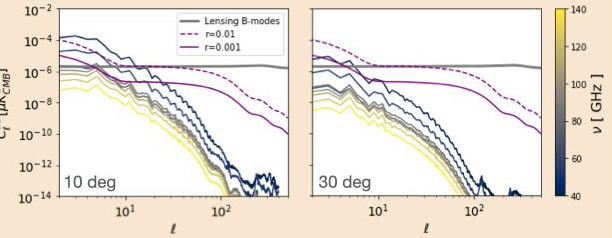


Figure2. B-mode spectra for a choice of frequency channels (see color bar) encoding (Left) far side lobe Galactic pick-up at angles> 10 deg, (right) >30 deg.

Calibration systematics

1. Simulated in TOAST:
 - Calibration mismatch:** random gain errors with Gaussian distribution during 24h observation for each detector .
 - Gain Drift:** Simulate a drift in the gain on long timescales with 1/f PSD for each detector.
2. Mitigation:
 - Following the NPIPE approach (See Planck intermediate results. LVII)
 - Fit gain systematics for each detector TOD as a linear combination of *Legendre polynomials* ($n<4$) assuming a scanned **template** map as an *estimate* of the signal.

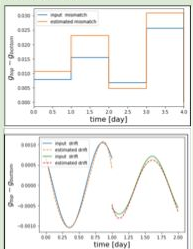


Figure 3. (top) Gain mismatches estimated (orange) compared with the one injected (blue) for one detector and 4 observations. (bottom) (solid) injected gain drifts, (dashed) estimated drifts.

3. **Simulation setup:** Frequency band 50 (12 detectors) and 140 GHz (48 detectors), 1 yr LiteBIRD scanning strategy
 - Gain mismatch: 1% mismatch every observation
 - Gain Drift: f_{knee}=20mHz, 10uK fluctuation amplitude

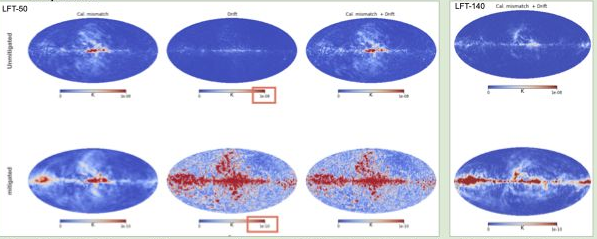


Figure 4. (Top) Polarized amplitude maps encoding unmitigated (bottom) mitigated systematic residuals from (first column) calibration mismatch, (second column) gain drift, (third column) both effects combined. (Maps are extra-smoothed to 2 degrees.)

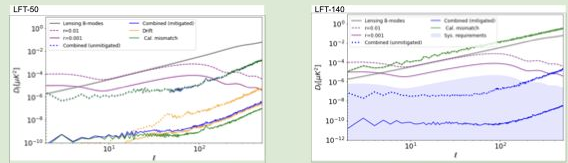


Figure 5. (Left) Power spectra for the simulations at 50GHz, encoding calibration mismatches (dotted green), gain drift (dotted orange), both combined (dotted blue). Post-mitigation residuals are shown as solid lines. (Right) power spectra for 140 GHz. We show in green the run encoding noise pre- (dotted) and post- (solid) mitigation. The noise-less runs encoding both calibration mismatch and gain drift are shown in blue. The blue shaded area show the requirement for systematic budget.

Cosmic Rays

- Using simulations 156 Hz of 16 detectors and 90 minutes of data. we characterize:
 - Direct hits.** Injecting glitches with an exponential profile „ given the expected rate of events. $\gamma(t) = C_1 + C_2e^{-t/\tau}$
 - Wafer noise:** simulate the low amplitude hits in the wafer as white noise signal with the specifics from simulation
 - Common mode noise:** correlated component for detectors within the same pixel
 - Simulation setup:** frequency channel at 119GHz, 3 years of observations, 16 pixels.
- Input signal: Cosmic rays only.



Figure6. Detector locations assumed in the physical simulations.

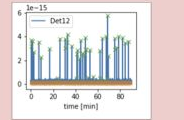


Figure7. (solid blue) 90 minutes of cosmic ray data for one detector. (green crosses) glitches detected with a peak finder. (solid orange) the wafer noise.

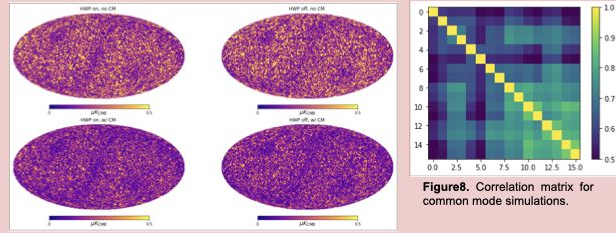


Figure9. Polarization amplitude maps obtained by simulating cosmic rays (glitches + wafer noise) for 1 detector pair and 1 year with Litebird scanning strategy (for the cases with (left) and without (right) HWP. Cosmic rays are simulated with (bottom) and without (top) a common mode. (Maps are extra-smoothed to 2 degrees to emphasize large scale structures) .

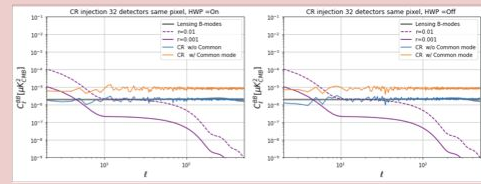
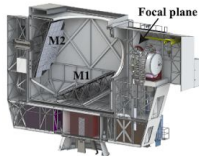


Figure10. B-mode power spectra for cosmic ray simulations with 16 pixels (see the inset) (solid blue) simulations performed without common mode, (solid orange) simulations encoding a common mode. (Left) panel refers to the case encoding a spinning HWP, whereas the case without HWP is shown in the right panel.

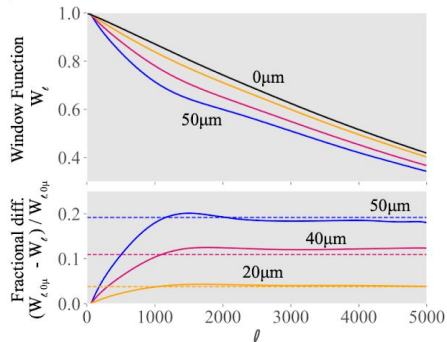
Simons Observatory

Simons Observatory (SO) is a millimeter-wave telescope with one Large Aperture Telescope (LAT) and three Small Aperture Telescopes (SAT) observing the cosmic microwave background (CMB) temperature and polarization signals from several degree to arc-minute angular scales [1].



Reflector Surface Defects

- SO is background limited, requires precise alignment of the reflectors.
- SO LAT surface error of $35\mu\text{m}$ HWFE leads to 10% loss in signal in $1000 < \ell < 5000$ range [2].
- Near-field radio holography is common method for mitigating surface defects in reflectors for millimeter and sub-millimeter experiments.

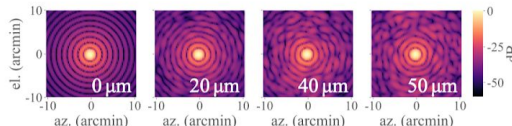


Top: Window function of far-field beams at 150 GHz with combined surface RMS of $0\mu\text{m}$, $20\mu\text{m}$, $40\mu\text{m}$, and $50\mu\text{m}$. Bottom: Difference of window functions in top plot, w.r.t. window function of far-field beam with surface error RMS of $0\mu\text{m}$ [2].

LAT Far-Field Beam Simulation

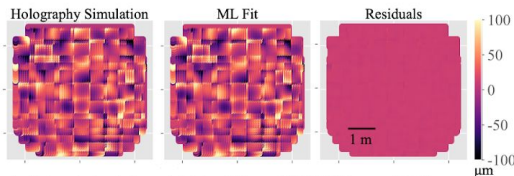
- Model misalignment of mirrors: surface z_{sur} for each mirror panel parameterized as polynomial of five parameters a_n :
$$z_{sur} = a_1 + a_2 r_x + a_3 r_y + a_4 (r_x^2 + r_y^2) + a_5 r_x^2 r_y^2$$
- Ray trace pathlength from points in aperture plane to source.
- Elevation θ and cross-elevation ϕ of this source are varied to map out the far-field beam $B(\theta, \phi)$:

$$B(\theta, \phi) = \sum_i E_i e^{i\rho_i(\theta, \phi) \cdot 2\pi/\lambda}$$



Machine Learning

- Train ML model (ordinary linear regression) with 1000 far-field beams and adjuster offsets.
- The residuals were computed for many input simulations with different realizations of adjuster errors.
- ML achieves HWFE residuals $< 3\mu\text{m}$ [2].

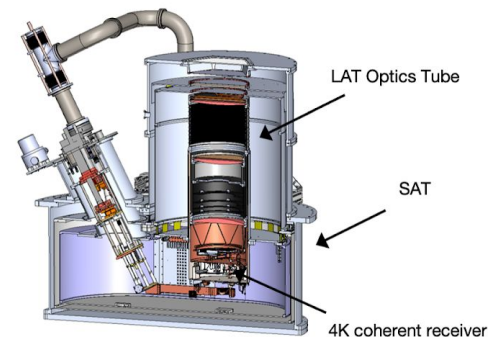


Left: input simulation which had $35\mu\text{m}$ RMS HWF error. Middle: predicted aperture phase given the ML determined estimates for the panel adjuster positions. Right: residuals [2].

LAT Receiver Tester

- LAT Receiver holds 13 40cm optics tubes (OT), with filters and three lenses and guiding CMB photons onto detector arrays [4].
- LAT Receiver Tester (LATrT): Adapted SO Small Aperture Telescope cools down LAT OT to 4K [3].

LATrT Setup



Beam Mapping with Holography

- Coherent millimeter-wave source scans in XY plane above front of OT.
- Harmonic mixer receives signal in focal plane.
- Holography beam maps will test the focus of the optics tubes, and optical systematics like scattering due to filters.

Acknowledgements

- [1] Galitzki et. al. SPIE, v.1070804, 2018.
[2] Chesmore et. al. in preparation.
[3] Harrington et. al. SPIE, v. 1145318, 2020.
[4] Xu et. al. SPIE, v. 1145315, 2020.

Abstract

We study here phantom models of dark energy represented by a scalar field and with tracker properties[1]. By means of a change of polar-like of variables, we study a general class of models classified in terms of a set of three free parameters. Upon comparison of the models with observations, our results suggest a preference for phantom-like dark energy and possibly a negative cosmological constant.

Introduction

Phantom scalar fields

One of the most amazing riddles in modern Cosmology is the existence of dark energy (DE), which is allegedly driving the present accelerated expansion of the Universe. Being the precise nature of DE unknown, it is common to assume that a scalar field ϕ can be the right candidate to explain its puzzling properties. Moreover, one cannot discard the possibility of phantom scalar fields, which are characterized by a phantom equation of state (EoS) w_ϕ with values beyond the so-called phantom divide: $w_\phi < -1$ [2].

In this work, we are interested in phantom fields with tracker properties, so that their EoS has attractor values at early times, which ameliorates the fine-tuning, but are also able to accelerate the cosmos expansion at late times. Examples of this are shown in Fig. 1, for different values of the model free parameters, and as a function of the scale factor of the Universe.

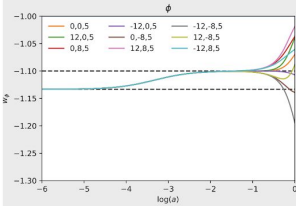


Fig. 1. Late time evolution of the phantom EoS for different values of the active parameters $\alpha_0, \alpha_1, \alpha_2$. The horizontal dashed lines represent the early-time tracker values during radiation and matter domination.

Tracker models of phantom dark energy

Mathematical background

We consider a spatially flat, homogeneous and isotropic universe described by the FRW metric filled with barotropic fluids and phantom scalar field ϕ endowed with a potential $V(\phi) + \Lambda$. For purposes of generality, the cosmological constant is part of the phantom energy budget. The Klein-Gordon equation of motion is $\ddot{\phi} = -3H\dot{\phi} + \partial_\phi V$, where H is the Hubble parameter. By means of a change to polar-like variables[3,4]:

$$\frac{\kappa\dot{\phi}}{\sqrt{6}H} \equiv \Omega_\phi^{1/2} \sinh(\theta/2), \quad \frac{\kappa V^{1/2}}{\sqrt{3}H} \equiv \Omega_\phi^{1/2} \cosh(\theta/2), \quad y_1 \equiv -2\sqrt{2} \frac{\partial_\phi V^{1/2}}{H},$$

the new equations of motion are: $\theta' = -3 \sinh \theta - y_1$, $y_1' = \frac{3}{2} \gamma_{tot} y_1 + \Omega_\phi^{1/2} \sinh(\theta/2) y_2$, $\Omega_\phi' = 3(\gamma_{tot} - \gamma_\phi) \Omega_\phi$. The free parameters of the phantom potential are encoded into the new function $y_2 = y(\alpha_0 + \alpha_1 y_1/\gamma + \alpha_2 y_1^2/\gamma^2)$.

The dynamics of the model depends on the values of the active parameters α . In particular, the tracker condition reads: $\gamma_\phi = -\gamma_{tot}/2\alpha_2$, where $\gamma_\phi = 1 + w_\phi$, $\gamma_{tot} = 1 + w_{tot}$ is the phantom (total) barotropic EoS. Thus, the tracker condition for phantom DE only requires $\alpha_2 > 0$. We show in Fig. 1 the evolution of the phantom EoS, $w_\phi = -\cosh \theta$ for different values of the triplet $\alpha_0, \alpha_1, \alpha_2$. The numerical solutions were obtained from an amended version of CLASS(v2.9.4)[5], where all other cosmological parameters were fixed to their Planck18 values.

Observational constraints on the models parameters

For a comparison with observations, we used MontePython(v3.3)[6] and measurements from BAO, Pantheon (SnIa), SH0ES and a compressed Planck18 likelihood[7]. In Fig. 2 we present the constraints on physical parameters for various models: Λ refers to the standard cosmological constant, $\phi + \alpha s$ is the phantom model with all α , $\phi + \alpha_2$ is the phantom model with $\alpha_0 = 0 = \alpha_1$, whereas $\phi + \Lambda + \alpha s$ and $\phi + \Lambda + \alpha$ refer to the same but with Λ as an additional free parameter, either positive or negative. Additionally, we have defined the effective DE EoS: $\gamma_{eff} = \gamma_\phi \rho_\phi / (\rho_\phi + \rho_\Lambda)$, to monitor any preference of data for a phantom EoS $\gamma_{eff} < 0$.

The main results can be summarized as follows. The cosmological parameters are well constrained and their mean values, in the case of the phantom models, differ a bit from those of Λ -only model, although in the case of $H_0 = 69^{+0.5}_{-0.6}$ the shift of the mean value is not enough to solve the Hubble tension. Also, the values of α_0, α_1 appear unconstrained, which means that the data cannot constrain more complexity in the phantom models beyond α_2 .

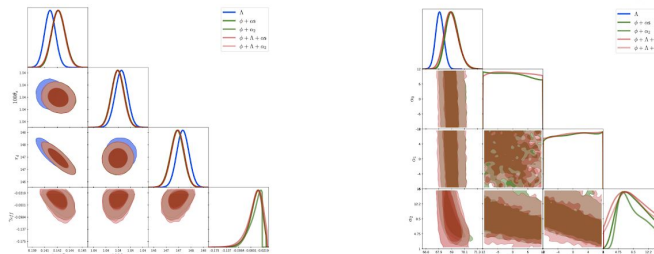


Fig. 2. (Left) Observational constraints on the matter physical density $\Omega_m h^2$, the acoustic scale θ_s , the dragging scale r_d and effective EoS of the DE budget γ_{eff} . (Right) Observational constraints on the Hubble parameter H_0 and the active parameters $(\alpha_0, \alpha_1, \alpha_2)$ that describe the phantom potential. See text for more details.

Conclusions

The data considered in this work suggest a preference for a phantom EoS (see Fig. 2), and in general we find that $\gamma_{eff} = -0.04^{+0.02}_{-0.01}$ and $\alpha_2 = 8.5^{+3.7}_{-4.4}$. We also show in Fig. 3 the constraints on Λ when taken as a free parameter in competition with all others in the phantom models. The posteriors distributions suggest a preference of a combined contribution of both phantom and Λ in the form $\Omega_\phi \simeq 0.9^{+0.3}_{-0.5}$ and $\Omega_\Lambda \simeq -0.2^{+0.5}_{-0.3}$.

To quantify the above preference, we used the code MCEvidence[8] and calculated the Bayes factors of the two phantom models against the standard Λ model. In any case, the result is $\ln B_{\phi\Lambda} \simeq +2$, which suggests Definite/Positive evidence in favor of the phantom models together with a negative cosmological constant.

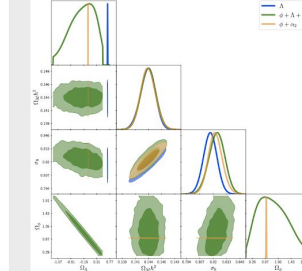


Fig. 3. Constraints on models containing Λ as a free parameter. The parameters are $\Omega_m h^2$, θ_s , Ω_ϕ and Ω_Λ .

References

1. F. Linares, N. Roy and L. A. Ureña-López, in preparation.
 2. Hao, Jian-gang and Li, Xin-zhou, Phys. Rev. D70, 043529 (2004).
 3. L. A. Ureña-López and N. Roy, Phys. Rev. D (2020), arXiv:2007.08873.
 4. N. Roy et al, Phys. Rev. D98, 063530 (2018), arXiv:1803.09204 [gr-qc].
 5. https://github.com/lesgourg/class_public.
 6. https://github.com/brinckmann/montepython_public.
 7. Arendse et al, Astronomy Astrophysics 639, A57 (2020).
 8. https://github.com/yatsuba/FantasyMCEvidence.
- Acknowledgements**
This work was partially supported by Conacyt-México (Grants: A1-S-17899, 304001), DAIP-UG, and PROMEP-UGTO-CA-3.

Mitigating the optical depth degeneracy using the kinematic Sunyaev-Zel'dovich effect with CMB-S4

Margaret Ikape | University of Toronto | with Renee Hlozek, Marcelo Alvarez, Simone Ferraro, J Colin Hill

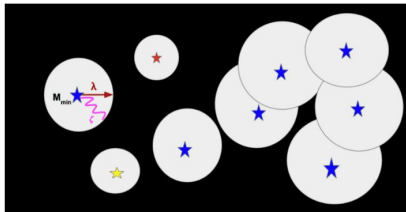


How did the first stars form, and what was their role in reionizing the universe?

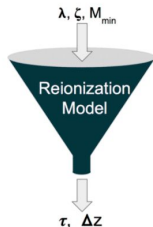
The universe is believed to reionize in patches and these patches grow as more atoms are converted to ions, and eventually overlap, until the whole universe is ionized.

Our simulation model [1] shows this process for a typical patch of the universe. The important parameters in this model are:

- **The efficiency, ζ** , which is the number of ionizing radiation the stars give off.
- **The mean free path, λ** , which is the average distance the radiation travels.
- **The mass, M_{\min}** of the stars causing reionization.



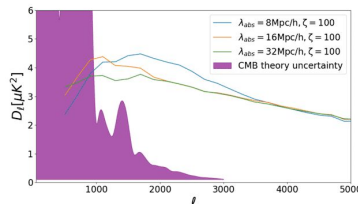
These parameters control the morphology and the history of reionization, and in turn tell us about the optical depth, τ and the duration of reionization, Δz .



Kinetic Sunyaev-Zel'dovich (kSZ) effect as a probe of reionization

The kSZ effect is the doppler boosting of CMB photons as they Compton-scatter off free electrons moving with a non-zero velocity.

This effect leaves an imprint on the CMB and careful study of this effect can provide enormous information about the EoR. The EoR kSZ signal depends sensitively on the astrophysical details of reionization, as it directly probes the distribution of free electrons. Varying the reionization parameters in the simulation produces various models of the kSZ power spectrum.



Constraints on the duration of reionization and optical depth.

We consider two statistical probes of the EoR kSZ signal:

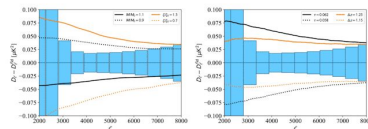
- The angular power spectrum (two-point function)
- A configuration of the trispectrum (four-point function) [2]

We compute the spectrum derivatives for the reionization parameters by varying the model parameters M_{\min} and ζ and then use the chain rule to compute $\frac{\partial C_\ell}{\partial \tau} = \frac{\partial \zeta}{\partial \tau} \frac{\partial C_\ell}{\partial \zeta} + \frac{\partial M_{\min}}{\partial \tau} \frac{\partial C_\ell}{\partial M_{\min}}$

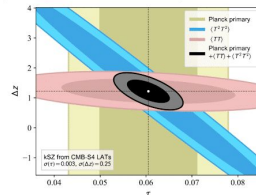
And similarly for Δz . Fixing $\lambda = 300$ Mpc/h, we perform a fisher analysis around a fiducial model with $\zeta = 70$ and $M_{\min} = 3 \times 10^9$ solar mass, which yields $\tau = 0.06$ and $\Delta z = 1.2$.

The kSZ two-point function and the reconstructed kSZ four-point function combined sufficiently breaks degeneracies between τ and Δz , yielding tight constraints on both parameters. We find $\sigma(\tau) = 0.003$ and $\sigma(\Delta z) = 0.25$ for a combination of CMB-S4 and Planck data.

Constraints on the duration of reionization and optical depth from CMB-S4 and Planck data.



The figure above shows the dependence of the kSZ power spectrum on reionization model parameters ζ and M_{\min} (left panel) and the resulting reionization history parameters τ , Δz (right panel). The shaded bars show 1σ uncertainties in the power spectrum including instrumental noise and residual foregrounds for a combination of CMB-S4 and Planck, and sample variance in the primary CMB and kSZ temperature for our fiducial model.



The vertical shaded contours are 68% and 95% confidence regions from the primary CMB anisotropies measured by Planck, which constrain the optical depth to an error of $\sigma(\tau) = 0.007$. The angled contours show forecast reionization constraints from the kSZ power spectrum (pink) and the kSZ four-point function (blue), as derived for CMB-S4 and Planck data. The black contours show forecast constraints from the combination of all three probes. The complimentary degeneracy directions of the two point and four-point function effectively break the degeneracy between the reionization parameters.

Works Cited

- [1] Alvarez, M. A., & Abel, T. (2012). The effect of absorption systems on cosmic reionization. *The Astrophysical Journal*, 747(2), 126.
- [2] Smith, K. M., & Ferraro, S. (2017). Detecting patchy reionization in the cosmic microwave background. *Physical Review Letters*, 119(2), 021301.



Mathieu Remazeilles

University of Manchester

Remazeilles, Rotti, Chluba, MNRAS (2021)

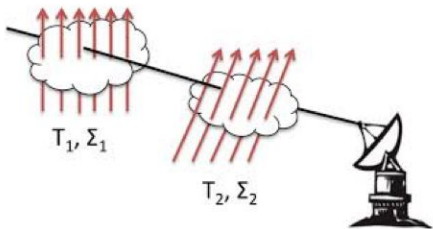
[arXiv:2006.08628](https://arxiv.org/abs/2006.08628)

cMILC (“constrained moment ILC”)

*Deprojecting foreground moments
with constrained internal linear combination
for B-mode component separation*

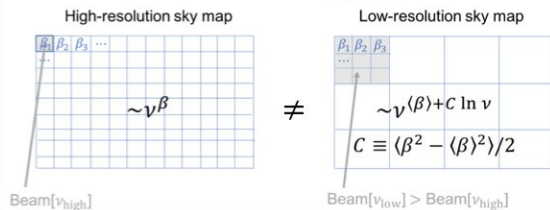
MOMENTS: distortions of baseline SED

Line-of-sight averaging



$$\nu^{\beta_1} B_\nu(T_1) + \nu^{\beta_2} B_\nu(T_2) \neq \nu^\beta B_\nu(T)$$

Beam averaging

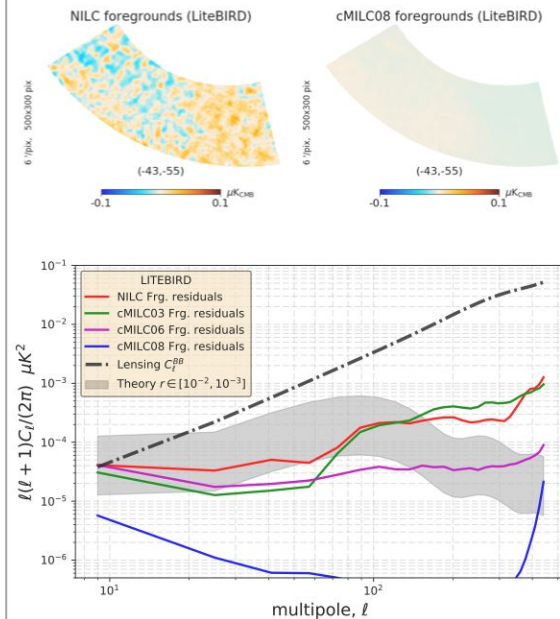


cMILC

$$\hat{s}_{\text{CMB}}(\vec{n}) = \sum_{\nu} w(\nu) \cdot d(\nu, \vec{n})$$

$$\left\{ \begin{array}{l} \sum_{\nu} w(\nu) \cdot f_{\text{CMB}}(\nu) = 1 \\ \sum_{\nu} w(\nu) \cdot f_{\text{sync}}(\nu) = 0 \\ \sum_{\nu} w(\nu) \cdot f_{\text{dust}}(\nu) = 0 \\ \sum_{\nu} w(\nu) \cdot \frac{\partial f_{\text{sync}}}{\partial \beta_s}(\nu) = 0 \\ \sum_{\nu} w(\nu) \cdot \frac{\partial f_{\text{dust}}}{\partial \beta_d}(\nu) = 0 \\ \sum_{\nu} w(\nu) \cdot \frac{\partial f_{\text{dust}}}{\partial T_d}(\nu) = 0 \\ \dots \end{array} \right.$$

FOREGROUND RESIDUALS



SHIFAN CHEN

An Emulator Combining Lagrangian Bias + N-Body Dynamics for Lensing-Galaxy Clustering Analyses

Traditional analyses use either simulations (expensive, empirical HODs) or perturbation theory (only at large scales). Can we combine their strengths?

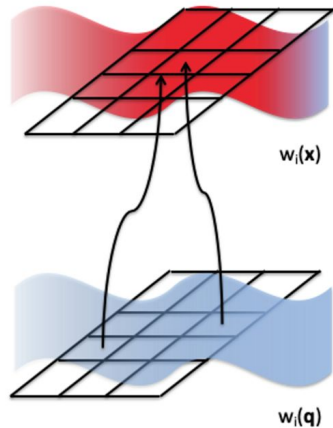
Yes! Use Lagrangian bias scheme + n-body particle displacements for galaxy-matter connection based on fundamental symmetries while resumming exact nonlinear dynamics.

Only need to emulate cosmology dependence of “components”—check out results using Aemulus simulations, including assembly bias and baryons.

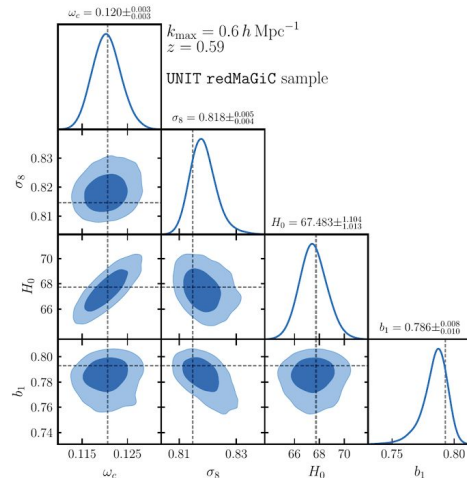
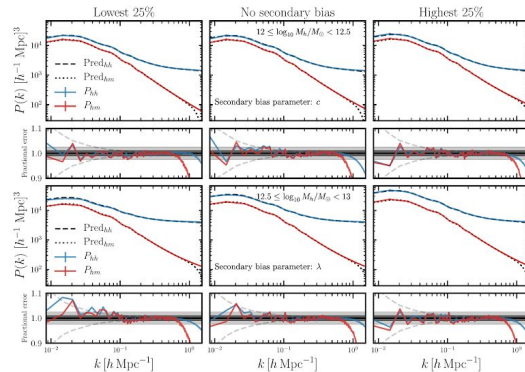
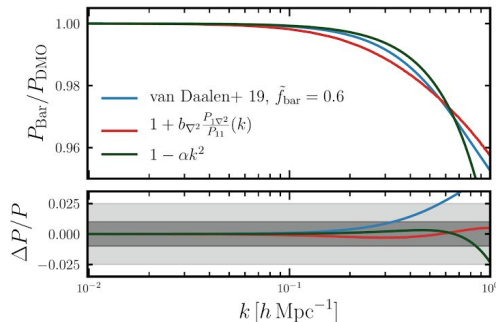
C. Modi, **SC**, M. White 2020 (1910.07097)

N. Kokron, J. DeRose, **SC**, M. White, R. Wechsler 2021 (2101.11014)

$$1 + \delta_g(\mathbf{x}) = \int d^3\mathbf{q} F(\mathbf{q}) \delta_D(\mathbf{x} - \mathbf{q} - \Psi_{\text{sim}})$$



$$F(\mathbf{q}) = \sum_{i=\{1, \delta_0, \delta_0^2, s_0^2\}} F_i w_i(\mathbf{q})$$

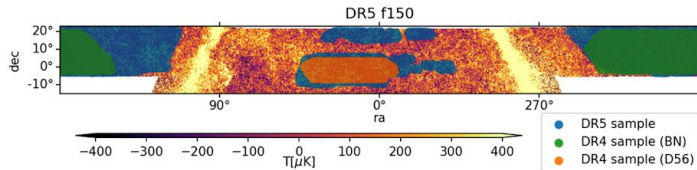


The Atacama Cosmology Telescope: Detection of the Pairwise Kinematic Sunyaev-Zel'dovich Effect with SDSS DR15 Galaxies arXiv:2101.08374

P. Gallardo, V. Calafut, E. Vavagiakis for the ACT collaboration.

Doppler shift of CMB-scattered light on a hot electron gas

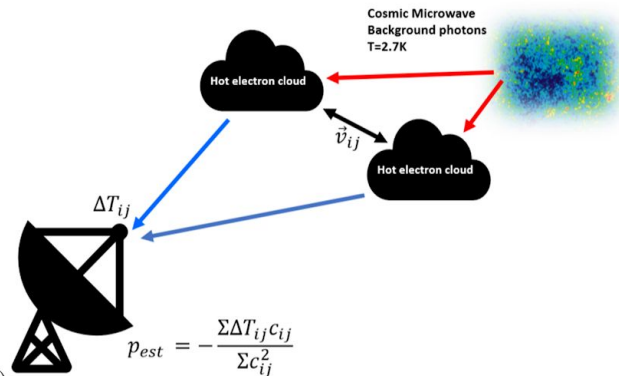
$$\frac{\delta T_{\text{KSZ}}}{T_0}(\hat{\mathbf{r}}) = - \int dl \sigma_T n_e \frac{\mathbf{v} \cdot \hat{\mathbf{r}}}{c}$$



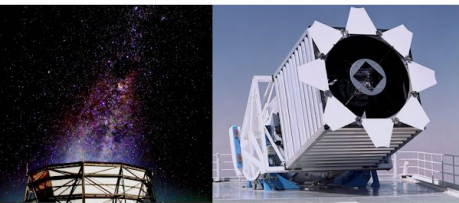
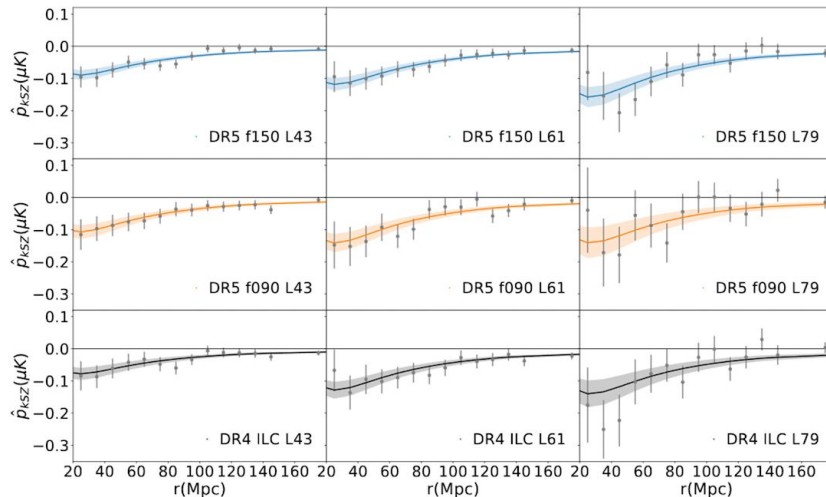
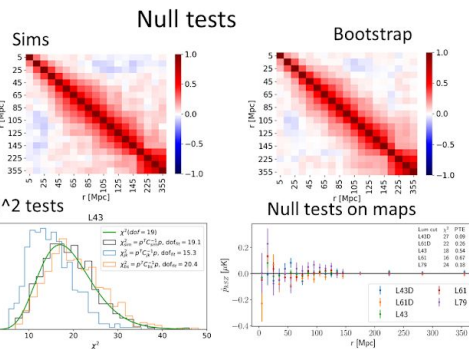
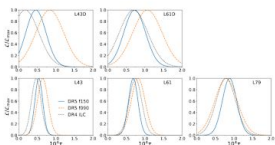
Small signal, use a statistical estimator

$$\hat{p}_{\text{KSZ}}(r) = - \frac{\sum_{i < j} (\delta T_i - \delta T_j) c_{ij}}{\sum_{i < j} c_{ij}^2}, \text{ extract } \tau \text{ by fitting}$$

$$\hat{p}_{\text{th}}(r, z) = - \frac{T_{\text{CMB}}}{c} \bar{\tau} V(r, z)$$



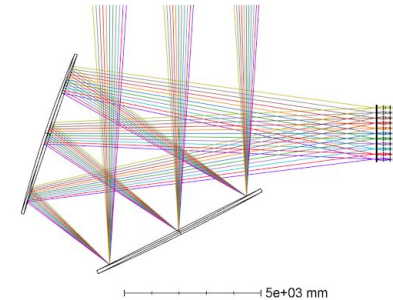
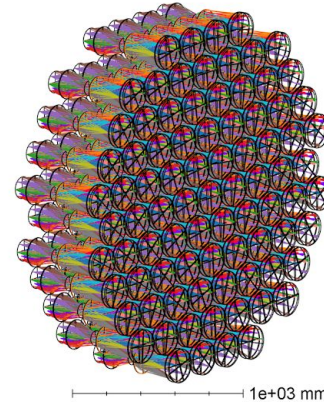
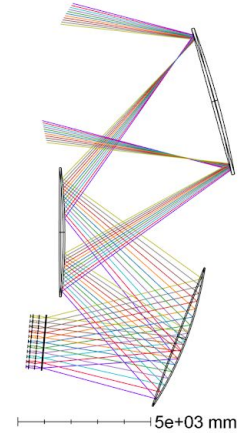
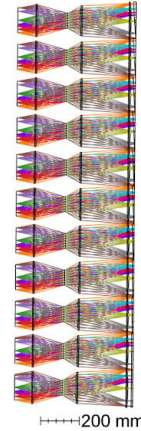
Tracer sample	DR4 ILC				DR5 f090				DR5 f150			
	$\bar{\tau} (\times 10^{-4})$	χ_{min}^2	PTE	SNR	$\bar{\tau} (\times 10^{-4})$	χ_{min}^2	PTE	SNR	$\bar{\tau} (\times 10^{-4})$	χ_{min}^2	PTE	SNR
L43D	0.18 ± 0.32	14	0.67	0.5	0.83 ± 0.34	12	0.81	2.2	0.46 ± 0.24	21	0.24	1.7
L61D	0.69 ± 0.34	25	0.08	1.8	1.07 ± 0.35	15	0.59	2.7	0.72 ± 0.26	11	0.85	2.5
L43	0.47 ± 0.12	22	0.20	3.6	0.65 ± 0.13	13	0.71	4.5	0.54 ± 0.09	17	0.42	5.1
L61	0.74 ± 0.15	18	0.40	4.4	0.82 ± 0.17	16	0.53	4.4	0.69 ± 0.11	10	0.92	5.4
L79	0.78 ± 0.23	21	0.21	3.0	0.79 ± 0.27	12	0.79	2.6	0.88 ± 0.18	13	0.76	4.6



Optical design of the 85-tube receiver for the CMB-S4 LAT.

Patricio Gallardo for the CMB-S4 LATR working group.

- The CMB-S4 receiver consists of 85 hexagonally packed optics tubes, composed of three plano-convex AR-coated silicon lenses and a silica wedge, which filters IR and corrects for tilt.
- The TMA LATR is composed of aspheric lenses, while the CD LATR is composed of biconic lenses.
- Studies are under way to define groups of cameras that share a similar optical prescription to minimize lens fabrication complexity.



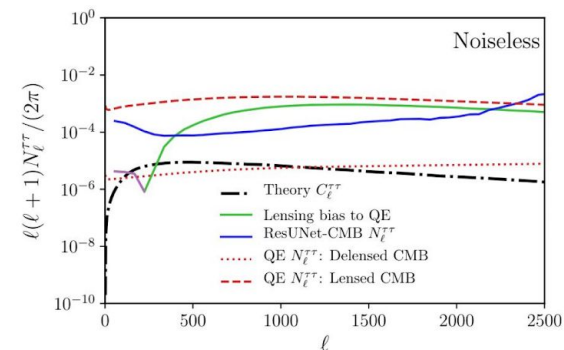
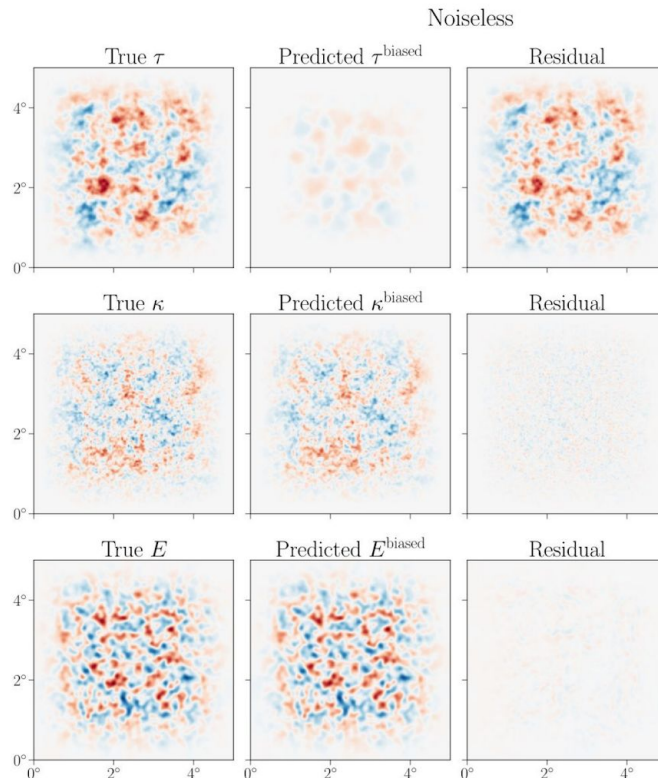
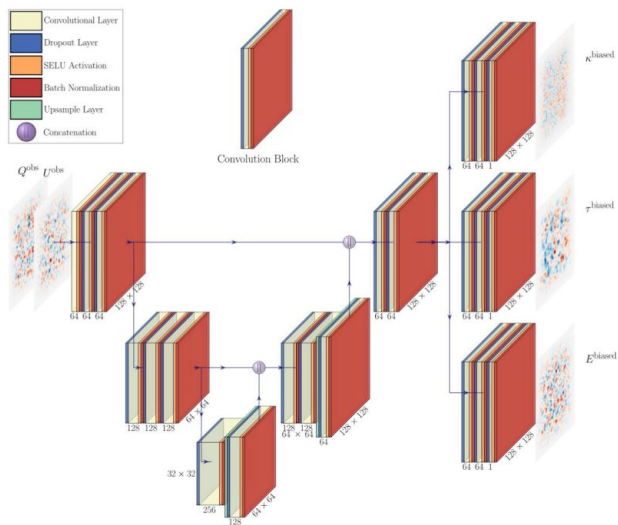
Reconstructing Patchy Reionization with Deep Learning

Joel Meyers
March 2021 Fireslide



Eric Guzman, 4th year
PhD Student at SMU

Based on Guzman, JM ([2101.01214](https://arxiv.org/abs/2101.01214))



See also Su, et al. (2011)

Future directions:

- Reconstruct other secondaries (e.g. cosmic birefringence)
- Treat realistic noise and foregrounds
- Combine with external datasets

<https://github.com/EEemGuzman/resunet-cmb>

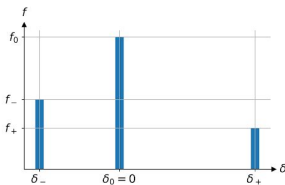
See also Caldeira, et al. (2019)

The idea

Jedamzik et al., 2020 showed that **small-scale baryon inhomogeneities** (clumping) induced by primordial magnetic fields **can relieve Hubble tension for Planck data**.

In this work, we propose a **generalization of their models**, and check how much better the effect is **constrained by improved CMB damping tail data from future CMB experiments**. For definiteness, we **assume that their power spectra continue to agree with standard Λ CDM model with $H_0 \approx 68$ km/s/Mpc**.

3-zone model (M3) for recombination



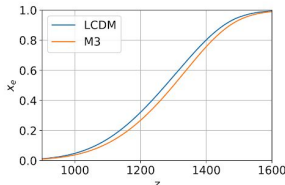
Need **6 parameters**: 3 weights (volume fractions) and 3 positions (densities). We set **3 constraints**: volume is preserved, mean density is preserved, and one of the densities is average. This leaves **3 free parameters**. We choose 2 other densities δ_{\pm} and one volume fraction f_0 .

For the sake of **generality**, we take **log-uniform priors for $|\delta_{\pm}|$** , **not assuming a particular scale of the effect**, and uniform prior for f_0 .

Toolkit

- CLASS (Blas et al., 2011) with M3 implementation – running RECAST (S. Seager et al., 1999; Sara Seager et al., 2000; W. Y. Wong et al., 2008) for each zone and then taking proper average x_i ;
- Polychord nested sampler (Handley et al., 2015a,b) and Py-BOBYQA minimizer (J. D. Powell, 2009; Cartis, Fiala, et al., 2018; Cartis, Roberts, et al., 2018) within Cobaya interface (Torrado et al., 2020);
- GetDist (Lewis, 2019) analysis tools;

Physical effect of clumping

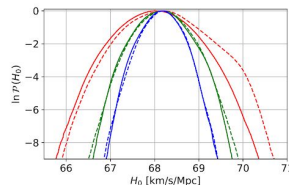


Inhomogeneities have $\langle n^2 \rangle > \langle n \rangle^2$, which enhances recombination rate. **Earlier recombination allows for higher H_0 for the same θ_*** . However, this **alters Silk damping scale** and therefore **CMB damping tail**.

Data

- Planck 2018: low- ℓ TT, EE, binned nuisance-marginalized high- ℓ TT, TE, EE (Aghanim et al., 2020a) and lensing (Aghanim et al., 2020b);
- Simons observatory (SO) (Ade et al., 2019) and CMB-S4 (Abazajian et al., 2019) models based on likelihood adapted from MontePython (Audren et al., 2013; Brinckmann et al., 2018), using deproj0 noise curves for T, E;
- SHES $H_0 = (73.2 \pm 1.3)$ km/s/Mpc (Riess et al., 2020), HOLCOW $H_0 = (73.3^{+1.5}_{-1.5})$ km/s/Mpc (K. C. Wong et al., 2019) and MCP $H_0 = (73.9 \pm 3.0)$ km/s/Mpc (Pesce et al., 2020), thereafter **H3**;

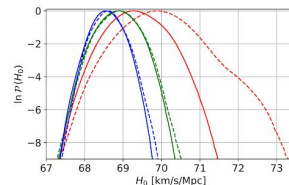
H_0 from CMB



H_0 [km/s/Mpc]	Planck18 (red)	SO baseline (green)	CMB-S4 (blue)
Λ CDM (solid)	68.02 ± 0.55	68.15 ± 0.39	68.16 ± 0.30
M3 (dashed)	68.19 ± 0.61	68.18 ± 0.39	68.18 ± 0.29

If future CMB experiments continue to agree with Λ CDM, M3 doesn't allow any significant H_0 shift.

H_0 from CMB+H3



H_0 [km/s/Mpc]	Planck18 (red)	SO baseline (green)	CMB-S4 (blue)
Λ CDM (solid)	69.33 ± 0.51	68.87 ± 0.38	68.57 ± 0.28
M3 (dashed)	69.91 ± 0.65	68.89 ± 0.38	68.61 ± 0.29

H_0 posterior with the joint data shifts to the value preferred by CMB, here assumed ≈ 68 km/s/Mpc.

Model comparison: M3 vs Λ CDM

	$\Delta\chi^2_{\text{best}}$	ΔAIC	$\Delta\log_{10} Z$
Planck18	1.2	-4.8	0.02 ± 0.12
Planck18+H3	14.8	8.8	0.76 ± 0.18
SO baseline+H3	0.2	-5.8	0.01 ± 0.21
CMB-S4+H3	0.7	-5.3	-0.11 ± 0.22

Planck is agnostic of M3. Planck+H3 prefer it. SO/CMB-S4+H3 also become agnostic.

Conclusion

Planck18 does neither prefer clumping significantly nor constrain it well. Additional pull from local H_0 measurements makes M3 beneficial with current data. Fine-tuned clumping parameters values allow for notably better fit, however, the whole posterior is affected not so much.

If SO and CMB-S4 results are also close to Λ CDM, clumping effects will no longer allow for significant raise of Hubble parameter. Otherwise, clumping will likely be confirmed with the new CMB data alone.

Source code

https://github.com/misharash/class_public
(CLASS fork with clumping implementation)
https://github.com/misharash/cobaya_mock_cmb
(mock CMB likelihood for Cobaya)
https://github.com/misharash/cobaya_H0_ext
(MCP and HOLCOW likelihoods for Cobaya)

Acknowledgements

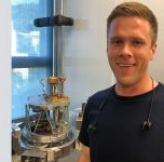
JBM was funded through a Clay fellowship at Smithsonian. DJE is partially supported by U.S. Department of Energy grant DE-SC0013718 and as a Simons Foundation Investigator. CD was partially supported by the Department of Energy (DOE) Grant No. DE-SC0020223.

Progress on Frequency Domain Multiplexed Readout of TES Bolometers with Sub-Kelvin SQUID Operation

Tucker Elleflot¹, Aritoki Suzuki¹, Chris Bebek¹, Kevin T. Crowley², Tijmen de Haan³, John Groh⁴, John Joseph¹, Adrian T. Lee^{1,2}, Joshua Montgomery⁴

¹ Physics Division, Lawrence Berkeley National Laboratory, Berkeley, CA, USA
² Department of Physics, University of California Berkeley, Berkeley, CA, USA

³ High Energy Accelerator Research Organization (KEK), Tsukuba, Ibaraki, Japan
⁴ Physics Department, NIST/University, Gaithersburg, MD, USA



INTRODUCTION

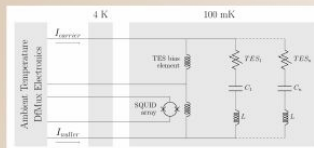
Digital Frequency Domain Multiplexing (DFMux) is a method of biasing and reading out many Transition Edge Sensor (TES) bolometers with an AC bias in the 1-5 MHz range using superconducting resonators and a Superconducting Quantum Interference Device (SQUID) array amplifier. DFMux has recently been deployed in two ground-based Cosmic Microwave Background receivers (POLARBEAR-2A, SPI-3G) with a multiplexing factor as high as 68 and is an alternative readout technology for the future ground-based experiment CMB-S4 and the baseline readout technology for the future satellite mission LiteBIRD.

The next generation of DFMux modifies the cryogenic circuit by moving the SQUID array and TES bias element from a dedicated 4 K carrier to a common carrier shared with the resonators at 100 mK, thereby reducing stray inductance in the electrical connection between them [1, 2]. This is expected to produce several benefits:

- Improved detector stability and linearity at low operating resistance
- Reduced and better controlled crosstalk
- Relaxed requirements on the 4 K to 100 mK cables

In addition to this change of the cryogenic architecture, future implementations of DFMux would benefit from the use of an optimized SQUID array with low input inductance, low dynamic impedance, and high transimpedance. These parameters play an important role in suppressing the noise of the SQUID array amplification chain in the DFMux system. An optimized SQUID array

Here we present the initial characterization of a prototype DFMux module implementing the improved cryogenic circuit architecture along with a demonstration of a first step toward an optimized SQUID array using existing SQUID series arrays.



- Each TES bolometer is placed in series with a resonant filter and biased with an alternating voltage of a unique frequency
- Optical power deposited on a TES modulates the amplitude of the bias current associated with that TES
- The bias currents from the multiplexed set of TES are summed and amplified by a SQUID array
- A nulling current is used to linearize the SQUID array response and reduce its input impedance

REFERENCES

1. de Haan, et al. "Recent Advances in Frequency-Multiplexed TES Readout: Vastly Reduces Parasitics and an Increase in Multiplexing Factor with Sub-Kelvin SQUID," *Journal of Low Temperature Physics*, Feb. 2020
2. Lowitz, et al. "Performance of a Low-Parasitic Frequency-Domain Multiplexing Readout," *Journal of Low Temperature Physics*, Feb. 2020
3. Boyd, et al. "SQUID array amplifier design strategies for CMB-S4," *Applied Superconductivity Conference*, Nov 2020

PROTOTYPE MODULE

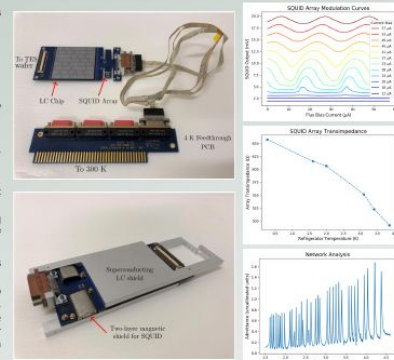
We have designed and fabricated several prototype readout modules implementing this new architecture (top left, bottom left).

Features:

- Compatible with POLARBEAR-2 (PB-2) cryostats and focal planes
- Controlled inductance trace to provide TES voltage bias
- Two-layer dedicated SQUID array magnetic shield
- No increase in effective SQUID array input inductance due to wirebonds or traces
- Solder pads for low-pass filter at SQUID input
- Compatible with several commonly used SQUID arrays (NIST SA13a, NIST SA4b, STAR Cycloelectronics E112)

The initial characterization of this system was performed in a test cryostat at Lawrence Berkeley National Laboratory (LBNL).

- Top right: Modulation curves of a SA13a SQUID array measured while the sub-kelvin fridge was cooled to its base temperature of 270 mK.
- Middle right: The SA13a SQUID array transimpedance increases as the temperature of the sub-kelvin refrigerator is lowered.
- Bottom right: A network analysis of a PB-2 40x resonator chip showing 35 resonant peaks. The resonators are terminated with 1 ohm resistors to mimic the normal resistance of PB-2 TESs. The five missing resonances are likely due to defects on the resonator chip or broken wirebonds and are not thought to indicate a problem with the prototype module.

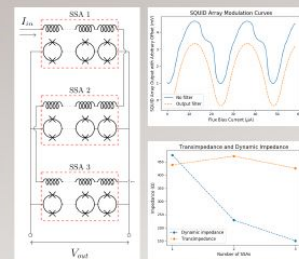


SQUID ARRAY WITH LOW DYNAMIC IMPEDANCE

As a step toward the development of an optimized SQUID array, we have demonstrated a method of combining several existing SQUID series arrays (SSA) to manipulate array parameters. Characterization of these prototype arrays were performed in test cryostats at LBNL and University of California Berkeley at approximately 4 K.

- Top left: Schematic showing the configuration of N SSAs (with N=3) under test that is expected to behave as a single array with parameters that scale with N:
- Dynamic impedance $\propto 1/N$
- Input inductance $\propto N$ (each SSA has a low input inductance of 11 nH, so a factor of a few increase is acceptable)
- Transimpedance constant
- Top right: Modulation curves of a prototype array with N=3. There are significant irregularities in its modulation curve, however a low-pass filter on the output of the array removed these irregularities.
- Bottom right: Transimpedance and dynamic impedance are plotted as a function of the number of SSAs used. The measured values match our qualitative expectations. Deviations from linearity are likely due to the fact that the SSAs used were not identical.

For more information on the development of an optimized SQUID array motivated in part by this work, see [3].



CONCLUSIONS

We have designed and fabricated a prototype DFMux module that integrates the SQUID array and resonator chip onto a single sub-kelvin carrier. The prototype design was adapted from the PB-2 cryogenic readout and thus is drop-in compatible with the PB-2 receivers and focal plane. Initial characterization of the prototype system is promising and the next steps will include a demonstration low noise TES performance using the prototype DFMux module

We have also laid the groundwork for the development of an optimized SQUID array by demonstrating a method of reducing the SQUID dynamic impedance while maintaining high transimpedance and low input inductance using existing SQUID series arrays. Work is ongoing to produce an optimized array based in part on this demonstration. Future work will include a stand-alone characterization of the optimized SQUID array and integration of the optimized array into the DFMux system at 100 mK.

Cryocooler for Use with a Two-Stage Pulse Tube

Tran Tsan¹, Nicholas Galitzki¹, Aamir Aif², Kam Arnold³, Gabriele Coppi³, Tamar Ervin⁴, Logan Foote², Brian Keating¹, Jack Lashner⁵, John Orlowski-Scherer⁶, Michael Randall¹, Joseph Seibert¹, Jacob Spisak¹, Grant P. Teply¹, Zhilei Xu^{3,7}, and Ningfeng Zhu⁸

¹Department of Physics, University of California, San Diego, La Jolla, CA 92038, USA, ²Department of Physics, University of California, Berkeley, Berkeley, CA 94720, USA, ³Department of Physics, University of Milano-Bicocca Piazza della Scienza, Milano (MI), Italy, ⁴Department of Physics and Astronomy, University of California, Los Angeles, Los Angeles, CA 90024, USA, ⁵Department of Physics and Astronomy, University of Southern California, Los Angeles, CA 90089, USA, ⁶Department of Physics and Astronomy, The University of Pennsylvania, Philadelphia, PA 19104, USA, ⁷MIT Kavli Institute for Astrophysics and Space Research, Massachusetts Institute of Technology, Cambridge, MA 02139, USA



INTRODUCTION

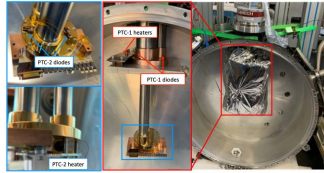
Pulse tube cryocoolers (PTCs) are frequently used to provide 40 K and 4 K stages as thermal shells in many ground-based CMB experiments. However, PTC operation is dependent on gravity, giving rise to changes in cooling capacity over the operational tilt range of pointed telescopes. We present a study of the performance of a two stage PTC with a cooling capacity of 2.0 W at 4.2 K and 55 W at 45 K (Cryomech PT420-RM) from 0-55° from vertical to probe capacity as a function of angle over a set of realistic thermal conditions. Our study provides a method to extract temperature given predicted thermal loading conditions across the angular range sampled. We then discuss the design implications for current and future tilted cryogenic systems.

TEST SETUP

We used Cryomech PT-420 with a remote motor variation for our tests. It was coupled with a CPA1114 Compressor.

Testing chamber

For our vacuum chamber, we used the front section of the MBAC. The PTC was mounted through an existing port. We installed a 1/2" thick aluminum radiation shield around the second stage to decouple the stage from the radiative environment. To minimize the radiative loading on the first stage, we wrapped 10 layers of MLI around the box and the first stage. The estimated radiative loading was 0.72 W and 0.07 μ W, respectively. The estimated loading from wiring on each stage was <0.3 W and <1mW, respectively.



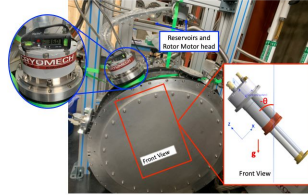
Heat application

- Stage-1: 2 diodes + A bank of five 100- Ω heaters in parallel (total resistance of 20 Ω), 0-51 W applied.
- Stage-2: 2 diodes + 500- Ω heater, 0-1.8 W applied.

METHODOLOGY

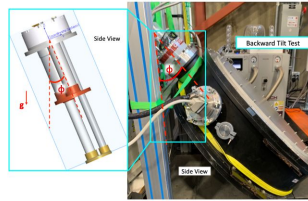
Tilt test:

- High density load curves with sparse angles:
 - Angles: 0°, 27.5°, 36°, 41°, and 48°.
 - Power: 6-12 W step for P_1 and <0.5 W step for P_2 .
- Sparse power but detailed angular steps (0-55°):
 - Angles: Every 6-8° until 40°, every 1-2° from 40-55°.
 - $P_1 = 0, 24, 51$ W. $P_2 = 0, 0.9, 1.8$ W.



Axis-dependency Check:

Since the geometry of the pulse is not symmetric, we rotated the chamber in positive and negative direction ($\pm\theta$) as well as a backward angle (ϕ) to check for any axis-dependencies. The figure above portrays where is θ with respect to the axis of the PTC, and the figure below illustrates the orientation of ϕ .



DATA REDUCTION

Data acquisition:

- Acquired data through SO Observational Control System (OCS)
- Applied power on the first stage (P_1) and iterated through P_2 . We then changed P_1 and repeated the process.

Data reduction:

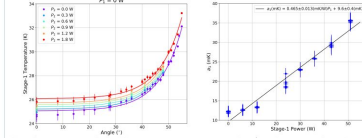
- Found the extrema at each loading step in the direction of stabilization.
- Selected all data within 2% of this extrema and got the median.
- Averaged the temperature between the 2 thermometers on each stage for the final values.

RESULTS

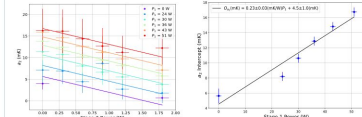
Performance vs inclination angle:

We fit the data to an exponential function below: $T_1(\theta) = a_1 e^{b_1 \theta} + c_1$.

- c_1 is the offset at 0° due the different power setting.
- b_1 is an angular scaling that is a property of the pulse tube and should be independent of loading. We constrained it to be the same across all the loading conditions.
- a_1 should be a function of the power on the stage.



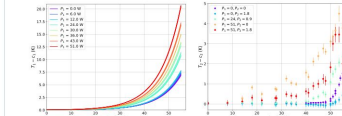
For Stage 1, we found $b_1 = 0.1157 \pm 0.0012 \text{ deg}^{-1}$ and a_1 as a function of P_1 . The (left) figure above illustrates the fits for $P_1 = 0$ W. The fits for other P_1 's are not here but you can see the fit results from the right plot of a_1 vs P_1 .



Stage-2 performance is more complex as a_2 depends on both P_1 and P_2 . In the figure, we plot a_2 vs P_2 and fixed the slopes for all P_1 set points (right). We then plotted the intercepts as function of P_1 (right).

Temperature uniformity over tilt angle:

We want to explore at what angle would the PTC experience a significant loss in cooling capacity. The spread of each color in the left plot is due to changing P_2 . Right plot illustrates the T data as the fits are less effective at capturing the trend at high angle. Depending on P_1 , the cooling power loss is not as prevalent in the first stage for angle less than 40° (< 3K). The trend on the second stage suggests that for the best temperature uniformity, one should try to minimize Stage-1 loading.



CONCLUSIONS

1. **Quantify performance vs angle:** We found an empirical model that describes the behavior on both stages of the PTC:
Stage 1: $T_1(\theta, P_1, P_2) = a_1(P_1) e^{b_1 \theta} + c_1(P_1, P_2)$
 $a_1(P_1) = 0.465 \left(\frac{\text{mK}}{\text{W}} \right) P_1 + 9.6 \text{ (mK)}; b_1 = 0.1157 \pm 0.0012 \text{ (deg}^{-1}\text{)}$
Stage 2: $T_2(\theta, P_1, P_2) = a_2(P_1, P_2) e^{b_2 \theta} + c_2(P_1, P_2)$
 $a_2(P_1, P_2) = -3.7 \left(\frac{\text{mK}}{\text{W}} \right) P_2 + 0.23 \left(\frac{\text{mK}}{\text{W}} \right) P_1 + 4.5 \text{ mK}$
 $b_2 = 0.101 \pm 0.006 \text{ (deg}^{-1}\text{)}$
2. **Temperature uniformity:** For telescope design requirements favoring temperature uniformity over wider tilt ranges, there is strong preference for lower stage 1 power and high stage 2 power.
3. **Rotational axis dependency:** More prominent on the first stage at high power and large angle, favoring - θ direction.

ACKNOWLEDGEMENT

This work was funded by the Simons Foundation (Award #547687, B.K.). Support from the Ax Center for Experimental Cosmology at UC San Diego is gratefully acknowledged.

REFERENCES

1. Gifford & Longworth, 1964
2. Radebaugh, 1999
3. Rie et al., 2013
4. Thummes et al., 1997
5. Ross & Johnson, 2004
6. Fang et al., 2016
7. Galitzki et al., 2018
8. Ade et al., 2019
9. Abazajian et al., 2019
10. Choi et al., 2020
11. Schell et al., 2020
12. Swetz et al., 2008

Massive neutrino non-standard interactions and the Hubble tension

Shouvik Roy Choudhury¹, Steen Hannestad², Thomas Tram²

¹Indian Institute of Technology Bombay (IITB), Powai, Mumbai, India-400076

²Aarhus University, Aarhus C, Denmark, DK-8000

Updated constraints on massive neutrino self-interactions from cosmology in light of the H_0 tension, arXiv: 2012.07519, accepted in JCAP

Abstract

We have updated the constraints on flavour universal neutrino self-interactions mediated by a heavy scalar, in the effective 4-fermion interaction limit. Based on the latest CMB data from the Planck 2018 data release as well as auxiliary data we confirm the presence of a region in parameter space with relatively strong self-interactions which provides a better than naively expected fit. However, we also find that the most recent data, in particular high- l polarisation data from the Planck 2018 release, disfavour this solution even though it cannot yet be excluded. Our analysis takes into account finite neutrino masses (parameterised in terms of Σm_ν) and allows for a varying neutrino energy density (parameterised in terms of N_{eff}), and we find that in all cases the neutrino mass bound inferred from cosmological data is robust against the presence of neutrino self-interactions. Finally, we also find that the strong neutrino self-interactions do not lead to a high value of H_0 being preferred, i.e. this model is not a viable solution to the current H_0 discrepancy.

Neutrino Self-interactions mediated by a heavy scalar

- In this paper we have updated the constraints from cosmology on flavour universal neutrino self-interactions mediated by a heavy scalar ($m_\phi \gtrsim 1$ keV), in the effective 4-fermion interaction limit (CMB temperature is far lower than the keV range).
- Simplified universal interaction: $\mathcal{L}_{\text{int}} \sim g_{ij} \rho_i \rho_j$ with $g_{ij} = g \delta_{ij}$.
- The effective self-coupling, $G_{\text{eff}} = g^2/m_\phi^2$ with $G_{\text{eff}} > G_F$ (Fermi constant), so that they remain interacting with each other even after decoupling from the photons at $T \sim 1$ MeV.
- The self-interaction rate per particle $\Gamma = n(\nu\nu) \sim G_{\text{eff}}^2 T_\nu^2$, where $n \propto T_\nu^3$ is the number density of neutrinos. Neutrinos don't free-stream until $\Gamma < H$.
- Introducing this kind of interaction had shown potential in solving the Hubble tension in previous works in the very strong interaction range ($G_{\text{eff}} \sim 10^6 G_F$) using older data.

The Cosmological Model of interest

- Cosmological model: $\Lambda\text{CDM} + \log_{10}[G_{\text{eff}}\text{MeV}^2] + N_{\text{eff}} + \sum m_\nu$.
- Kreisch et al., Phys. Rev. D 101, 123505 (2020) found the 68% bounds: $\log_{10}[G_{\text{eff}}\text{MeV}^2] = -1.41^{+0.26}_{-0.20}$ (strong self-interactions), $H_0 = 71.1 \pm 2.2$ km/s/Mpc, $N_{\text{eff}} = 3.80 \pm 0.45$, $\sum m_\nu = 0.80^{+0.30}_{-0.20}$ eV.
- With **Planck 2015 low- l and high- l TT+lensing** combined with BAO, with similar goodness of fit to the data as ΛCDM .
- In this model, N_{eff} and H_0 are **positively correlated** \rightarrow Solution to the Hubble tension came from high $N_{\text{eff}} \simeq 4$ values.
- Planck polarization data was not used for main conclusions.
- With the **public release of the Planck 2018 likelihoods**, we thought it is timely to test the model again.
- We made runs which incorporated the full prior range of $\log_{10}[G_{\text{eff}}\text{MeV}^2]$, i.e. $-5.5 \rightarrow -0.1$.
- We also run the non-interacting case (N_{eff}), the moderately interacting case $\text{M}\nu$ ($\log_{10}[G_{\text{eff}}\text{MeV}^2] \lesssim -2$), and the strongly interacting case ($\text{S}\nu$) ($\log_{10}[G_{\text{eff}}\text{MeV}^2] \gtrsim -2$) separately.

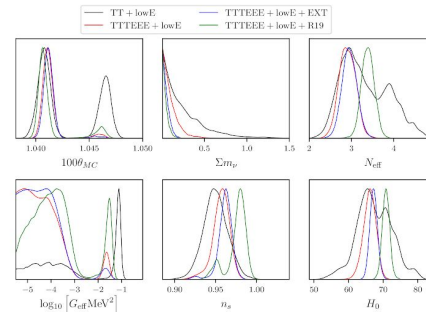
1 Datasets

- Cosmic Microwave Background, Planck 2018:** low- l and high- l temperature data, TT, TT plus high- l ($l \geq 30$) TE + EE-mode polarization data: **TTTEEE**, low- l E-mode polarization data: **lowE**.
- EXT** \equiv Planck 2018 lensing + BAO + RSD + SNe Ia.
- R19** \equiv Gaussian prior on the Hubble constant from direct measurement (Riess et al., 2019) which is $H_0 = 74.03 \pm 1.42$ km/sec/Mpc. (1.4 σ tension with Planck 2018 in ΛCDM). This has changed to $H_0 = 73.2 \pm 1.3$ km/s/Mpc in 2020.

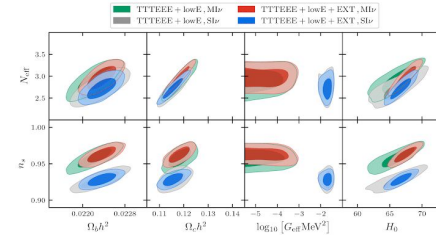
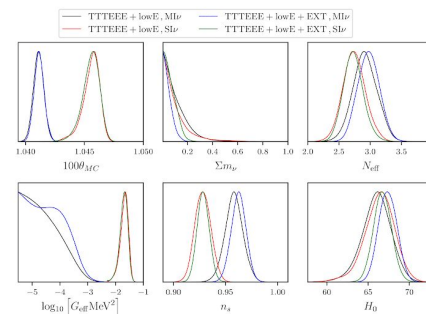
Results

1.1 Plots from runs with full prior range of $\log_{10}[G_{\text{eff}}\text{MeV}^2]$

Main conclusions follow from the **TTTEEE+lowE+EXT** dataset (blue curve).



1.2 Mode separation: M ν and S ν plots shown separately



Discussion

- $\log_{10}[G_{\text{eff}}\text{MeV}^2]$ is degenerate with θ_{MC} and n_s . This allows for a bimodal posterior distribution, even with the latest full Planck data.
- $\log_{10}[G_{\text{eff}}\text{MeV}^2]$ is also degenerate with both N_{eff} and $\sum m_\nu$ in the TT data. This allows for high N_{eff} and thus high H_0 values as long as **Planck 2018 polarization data is not included**.
- However including the polarization data constrains N_{eff} heavily and thus doesn't lead to high H_0 values that can reconcile CMB data ($H_0 \simeq 67$ km/s/Mpc in the ΛCDM model) with local universe measurements ($H_0 \simeq 74$ km/s/Mpc), which have a 4 σ tension.
- With **TTTEEE+lowE+EXT** we found the following **95% bounds**, for the $\text{S}\nu$: $H_0 = 66.7^{+2.1}_{-2.2}$ km/s/Mpc, $N_{\text{eff}} = 2.73^{+0.11}_{-0.10}$, $\sum m_\nu \leq 0.15$ eV.
- Even if one were to re-analyze the data with a fixed $N_{\text{eff}} = 3.04$ with massive neutrinos and strong interactions, one would very likely get H_0 values in the ballpark of $60 - 70$ km/s/Mpc (as can be seen from the plots above), which does not work as a solution to the Hubble tension, albeit reducing the tension slightly compared to vanilla ΛCDM .
- For the Non-interacting case ($\text{N}\nu$: $\Lambda\text{CDM} + N_{\text{eff}} + \sum m_\nu$), we find $H_0 = 67.3 \pm 2.2$ km/s/Mpc (95%) \rightarrow The strongly interacting model doesn't work better than this simple extension to ΛCDM .
- Furthermore, **Neutrino self-interactions are also strongly constrained from particle physics experiments**, with the exception of flavour specific interaction among the τ -neutrinos. Introducing the interaction realistically only in one flavour would provide an even smaller increment to H_0 (as the effect on CMB power spectra will be smaller).
- We find, $-2 \log_{10}(\mathcal{L}_{\text{S}\nu}/\mathcal{L}_{\text{N}\nu}) = 3.4$ (approx. $\Delta\chi^2$), and $Z_{\text{S}\nu}/Z_{\text{N}\nu} = 0.06$ (evidence ratio), with **TTTEEE+lowE+EXT**.
- Bayesian evidences and log likelihood values both **disfavour very strong self-interactions** compared to $\Lambda\text{CDM} + N_{\text{eff}} + \sum m_\nu$, i.e. the non-interacting scenario $\text{N}\nu$.
- However, the moderately interacting mode $\text{M}\nu$ gives similar fit to the data as $\text{N}\nu$, and leads to almost similar parameter constraints to $\text{S}\nu$. The reason is for the $\text{M}\nu$ coupling strength, neutrinos start free-streaming too early and affects lower scales than what Planck measures.
- One can vary Y_ν (He abundance), but current bound $Y_\nu = 0.2445 \pm 0.0010$ (68%) from CMB+BBN are quite tight, even with varying N_{eff} (Fields et al., JCAP03(2020)010, arXiv: 1912.01132). So there is not much wiggle room in the parameter space.
- To conclude, with current data, the strong neutrino self-interaction model does not look like a promising solution to the current H_0 discrepancy.

Potential for Radio Frequency Interference from Satellite Constellations in CMB-S4 Projects

Ian Birdwell, Darcy Barron, CMB-S4 RFI Working Group (Chair: Scott Paine)

Introduction

Radio frequency interference (RFI) is an ongoing issue in observational astronomy. Interference may arise from telecommunications infrastructure (satellite- or ground-based), Earth exploration satellites, or broadcast technology. To prevent RFI from disrupting observation, it is necessary to characterize and model its impact. Satellite RFI has typically been limited by the relatively low number of satellites capable of strong emission.

Recently, satellite constellations (such as SpaceX) have begun to acquire permissions to operate within certain bandwidths of interest to the CMB-S4 collaboration. In particular, SpaceX has been licensed to operate its Starlink satellites in the ranges of

10.7-12.7 GHz,
17.8-18.6 GHz,
18.8-19.3 GHz, and
37.5-42.0 GHz

for space-to-Earth functions.

These constellations may not break new ground in terms of expected power flux density (EPFD), as they are limited by ITU limits on such figures. The number of satellites in these constellations prompts concern - projections run into the tens of thousands, with over 1,000 Starlink satellites deployed already.

Model Description

The model constructed addresses Starlink usage of the *Ka* band. An overview of possible RFI candidates, for comparison and scale, was overlaid with transmittance values at the South Pole and Chile sites using annual median climate data. (Fig. 1). Cambridge, MA was included to provide a control of Starlink's client base. Of particular interest were broadcast satellites, active Earth exploration satellites, and "fixed satellites", representative of most concerning satellites. Effective isotropic radiated power was given an upper limit (-11.07 dB-W/4KHz); using transmittance values for Cerro Toco in Chile at various angular altitudes (and using the only present orbital height of ~550 km), expected power coupling estimates were produced (Fig. 2).

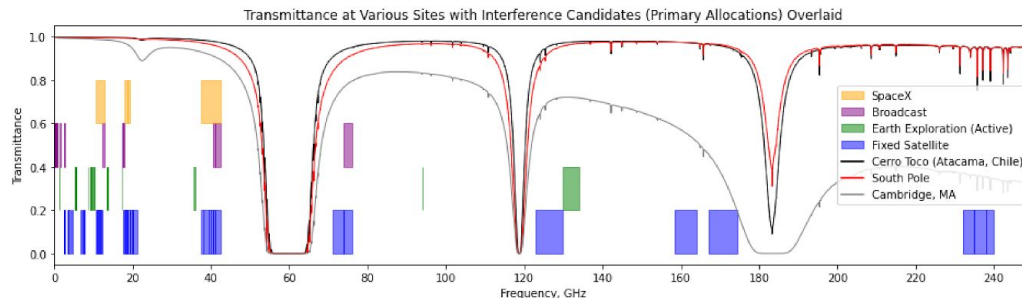


Fig. 1, above: Transmittance and Allocations

This plot shows, as boxes, SpaceX approved operations frequencies (yellow, top), broadcast satellites (purple, second from top), active Earth exploration satellites (green, third from top), and fixed satellites (blue, bottom). Most telecommunications constellations (Starlink, OneWeb, etc.) will likely fall within the fixed satellite allocation due to infrastructure. Transmittance is plotted for Chile and South Pole sites to allow comparison with CMB-S4 observation windows. A transmittance line for Cambridge, MA provides a control - perhaps it may be less likely for constellations to utilize bands above *Ka* due to reduced atmospheric transmittance.

Fig. 2, right: Power Received

Using the model constructed, and assuming 0 dBi coupling to sidelobes, estimates can be made regarding the signal power observed by a detector. In this case, it is worth comparing these figures to an optical background power of 1.1 pW, and a saturation power of 2.8 pW for telescopes observing in this range.

Conclusions

Fig. 1 illustrates the territory which may be covered by future telecommunications constellations, with proximity to areas of interest to CMB-S4 projects. It is a recommendation to remain abreast of future allocations granted to satellite constellations. Fig. 2 shows estimates of how a detector may observe RFI within the *Ka* band, providing figures which may be more relevant to some instruments than others based on operations. However, these estimates rely on figures in literature, and may have variation in practice; thus, it is a recommendation to profile noise at this stage to better understand how future CMB-S4 projects may correct for this noise in observation strategy, instrument design, or data processing.



References

FCC DA 21-34

Xia, Shiyi et al. (2019, December 26). "Beam Coverage Comparison of LEO Satellite Systems Based on User Diversification." *IEEE Access*.

Paine, Scott. (2019, September 12). "The am atmospheric model (Version 11.0)".

Full resources and working group information at: <https://ghz.unm.edu/ibirdwell.html>



Ali CMB Polarization Telescope

Maria Salatiño, on behalf of the AliCPT collaboration
Stanford University & KIPAC, marias5@stanford.edu

The SCIENCE

Ali CMB Polarization Telescope (AliCPT): the first CMB polarimeter in the Tibetan Plateau.

- Target: Cosmic Microwave Background (CMB) polarization, lensing spectrum, cosmic birefringence, foregrounds
- Northern Hemisphere
 - Different patch of the sky, with respect to Atacama desert and the South Pole
- Overlap with the Atacama desert and DESI

AliCPT and CMB-S4

- Unique opportunity of cross-observations with CMB-S4
- Unique facility in the Northern Hemisphere
- Instrument design similar to CMB-S4 Small Aperture Telescope

The SITE and the MOUNT



Fig. 1 The AliCPT site.



Fig. 2 The mount (left), environmental seal and the green wind break (right).

- Ngari (Ali) site in the Prefecture of Tibet (Fig. 1)
- 32°18'38" N, 80°01'50" E at 5,250m above sea level
- Precipitable Water Vapor (PWV) quartiles: 0.87/1.34/2.125 (1)
- Mount developed by IHEP (Fig. 2)
- scanning in azimuth at constant elevation
- (45°-70°) elevation range
- up to 4"/s scanning speed
- environmental seal and wind break (Fig. 2)

The AliCPT RECEIVER

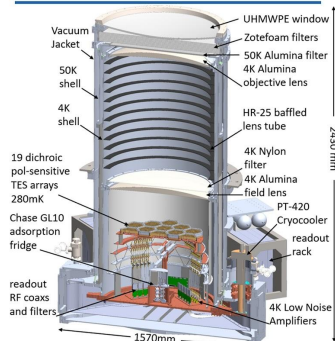


Fig. 3 SolidWorks model of the AliCPT receiver.

- A two-lens refractive telescope cooled down to 4K with 32,376 Transition-Edge Sensors (TESes) (2)
- Cryostat and optics: up to 19 TES arrays
- Kilopixel focal plane camera (3)
- Cryomech PT420 pulsetubes
- Custom Chase GL10 adsorption fridge
- Instrument and detector design heritage: BICEP3 (4) and AdvACT, respectively

OPTICS and AR COATING

- f/1.4 camera, telecentric focal plane
- 800 mm diameter alumina ceramic lenses
- 20.8°-33.4°; 7°-19-TES arrays field of view
- 380-636 mm diameter 7°-19-TES arrays focal plane
- Filters
 - 12mm thick UHMWPE window
 - Zotefoam and Nylon 50K and 4K infrared-blocking filters
- Anti Reflection (AR) coating
 - 2-layer Stycast epoxy (4,5)
 - flat sheets of precise thickness casted in a mold
 - lens profile formed softening sheets in an oven
 - target: mean surface reflections <1% per surface

Note: this poster is based on the one that has been presented at the SPIE Astronomical Telescopes + Instrumentation 2020

DETECTORS and READOUT

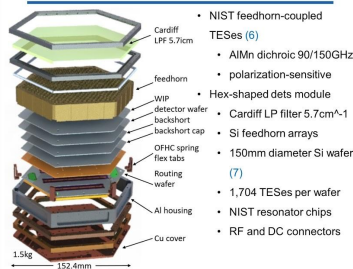


Fig. 4 SolidWorks model of the AliCPT detector module.

Frequencies	90GHz	150GHz
center frequency (GHz)	91.5	145
bandwidth (GHz)	33.0	34.0
Pixels number	16,188	16,188
P _{avg} (μW)	6.0	7.0
G _{eff} (μW/K)	60.96	70.95
NEP Photons (aW/√Hz)	17.9	19.4
NEP Photons (aW/√Hz)	50.6	61.0
NEP Total (aW/√Hz)	53.7	64.0
Resolution (FWHM)	19°	11°
NET CMB (μK/√s)	369.5	435.2

Tab. 1 AliCPT TESes specs.

- Frequency-division multiplexing architecture with SQUID-coupled 4-6 GHz resonators (μmux) (8)
 - current: 896 multiplexing (MUX) factor
 - under development: full 4-8 GHz band, MUX target: 2,000
- Cold multiplexing readout
 - 4K and 50K ASU Low Noise Amplifiers
 - SS, NbTi, Cu coaxes: RF lines
 - Manganin, NbTi cables: DC lines (TES bias and flux ramp)
- Warm readout electronics
 - Xilinx's ZCU111 RFSOC, open source
 - BLAST-TNG style firmware (9)

CURRENT STATUS

- Mount being commissioned on site.
- Receiver under integration and test at Stanford.
- TES array design and fab at NIST, μmux readout under development at ASU and NIST.

REFERENCES

- Kuo C.-L., *ApJ* 848, 1, 2017
- Salatiño M. et al., *SPIE* 11453, 2018
- Salatiño M. et al., to be published in *IEEE Trans. On Appl. Supercond.*
- Ahmed Z. et al., *SPIE* 9153, 2014
- Inoue Y. et al., *Appl. Opt.* 53, 2014
- Li D. et al., *JLTP* 184, 66, 2016
- Duff S. et al., *JLTP* 184, 634, 2016
- Mates J., *PhD thesis*, 2011
- Gordon S. et al., *Astr. Instr.* 2016

Inference of τ from low- ℓ temperature and polarisation *Planck* data



Roger de Belsunce with Steven Gratton, Will Coulton & George Efstathiou

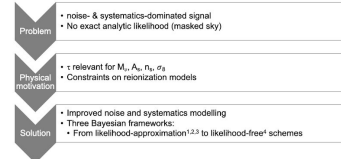
Institute of Astronomy and Kavli Institute for Cosmology, University of Cambridge

Summary

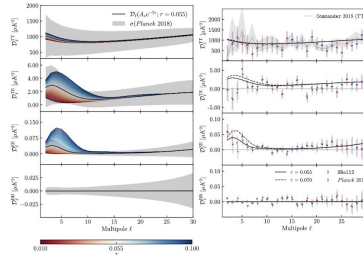
We present an updated constraint on the optical depth to reionization, τ , using cosmic microwave background (CMB) data from the High Frequency Instrument of the *Planck* satellite. We measure τ using foreground cleaned 100 and 143 GHz full-mission *Planck* 2018 (Sroll1) and Sroll2 frequency maps at low multipoles ($2 \leq \ell \leq 29$). Through the use of realistic, correlated

noise modelling, a rigorous handling of large-scale systematic modes and a quadratic cross power spectrum estimator we obtain a reliable error budget and an unbiased estimate of τ . We compare three likelihood approaches: a simulation-based likelihood, a likelihood-approximation and a density-estimation likelihood-free scheme, finding consistent constraints.

Motivation



Measure τ on 100x143GHz *Planck* low- ℓ HFI maps



Joint likelihood for τ using TT, TE & EE data

Conclusions

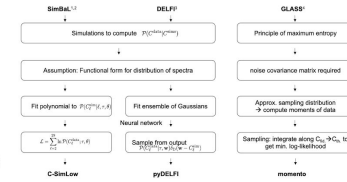
1. Consistent results for three Bayesian methods
2. Tighter constraints than Planck 2018/SR012
 1. Improved noise & systematics modelling
3. First joint likelihood TT, TE & EE for τ

References

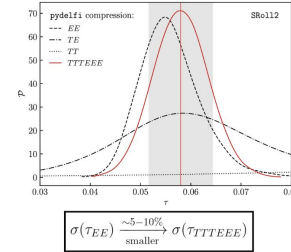
- [1] Planck Collaboration XLVI (2016)
 [2] Pagano et al. (2020)
 [3] Gratton (2017)
 [4] Alsing et al. (2018)

From likelihood approximations to

likelihood-free inference



Results



Likelihoods	CanSpec + momento (EE)	CanSpec + momento (TTEEE)
	<i>Planck</i> 2018	
τ	$0.0508^{+0.0056}_{-0.0062}$	$0.0536^{+0.0051}_{-0.0060}$
$\ln(10^{10} A_s)$	3.035 ± 0.013	$3.039^{+0.011}_{-0.013}$
z_{re}	7.37 ± 0.62	7.56 ± 0.57



Abstract

Context : Extracting unbiased all-sky thermal Sunyaev-Zeldovich (tSZ) effect maps from multi-frequency CMB data is important for both cosmology and astrophysics. The tSZ power depends strongly on some cosmological parameters ($C_l \sim \sigma_8^2 (\Omega_b h)^2$), providing useful constraints on cosmic structure formation. It is also highly sensitive to baryonic feedback processes in galaxy groups and clusters. In this study, we try to quantify the CIB leakage in tSZ maps for two experiments SO and SO+FYST combined.

Results : Using a simple ILC method on a mock sky containing only tSZ, CIB, and instrumental noise. We find that the cumulative CIB and instrumental, ILC residual noise left in tSZ is 18% less important when SO and FYST are combined rather than for SO alone. When we add galactic dust to the mock sky, this number rises to 26%.

Next steps : Make the mock sky more realistic by including all the components of the microwave sky. Improve our components separation method, for example, use CILC and quantify the noise penalty. Quantify the CIB bias.

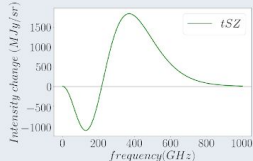
What are the tSZ effect and CIB ?

The thermal Sunyaev-Zeldovich (SZ) describe the energy change generated by the inverse Compton scattering of CMB photons on the hot electrons in galaxy clusters :

$$\frac{\Delta T_{CMB}}{T_{CMB}} = y(x_\nu \frac{e^{x_\nu} + 1}{e^{x_\nu} - 1} - 4) \quad (1)$$

Where $x_\nu = \frac{h\nu}{k_B T_{CMB}}$, $y = \int \frac{k_B T_e}{m_e c^2} n_e \sigma_T dl$

The Cosmic Infrared Background (CIB) is due to the photons emitted by stars and galaxies being absorbed by dust and re-emitted in the infrared domain.



Why is there CIB leakage in tSZ ?

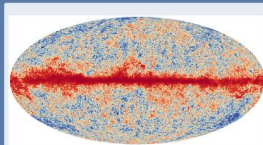
The tSZ signal originates in galaxy clusters, which is also the case for the stars and galaxies emissions generating the CIB. For this reason, the two signals are correlated. When performing an ILC part of the CIB signal leaks into the resulting tSZ map. The goal is to quantify how much CIB residual can be improved using SO+FYST.

FYST and SO telescopes

- **Fred Young Submillimeter Telescope (FYST)** : will be a 6-meter diameter, wide field-of-view telescope built at 5600m in Chile, first light is expected for ~2023.
- **Simons Observatory (SO)** : will be a 6-meter diameter telescope built in Chile. Its model is identical to FYST but its frequency coverage is slightly lower.

Frequency (GHz)	beam FWHM (arcmin)	Sensitivities SO (μK_{CMB} -arcmin)	Sensitivities FYST (μK_{CMB} -arcmin)
93	2.2	8	—
145	1.4	10	—
220	1.0	22	15
280	0.9	54	27
350	0.6	—	105
405	0.5	—	372
860	0.2	—	5.7×10^3

Microwave sky model

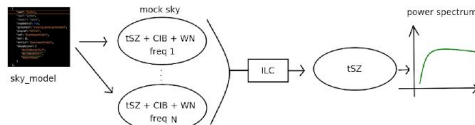


Code producing high-resolution full-sky maps of the microwave sky at a given frequency between [27GHz,860GHz]. The Galactic components are produced using PySM (Thorne et al 2017) and the extragalactic components using templates from simulations CITA WebSky (Stein et al 2020).

Code fully available on Github : https://github.com/MaudeCharmetant/CCATp_sky_model

Method

- Use simulations to generate maps of tSZ+CIB+Instrumental Noise.
- At SO and FYST frequencies, sensitivities, and beams.
- Applying ILC on them to extract a tSZ map, take its power spectrum.



Internal Linear Combination (ILC)

ILC is a multi-frequency component separation method that allows retrieving one component of choice. It is a 'blind' method because no information other than on the component of interest is needed. The hypotheses are:

- All components have to be uncorrelated
- Observations are a linear combination of the component of interest + noise :

$$T_i(p) = a_i s(p) + n_i(p) \Rightarrow s_{ILC} = \sum_i \omega_i T_i(p) \quad (2)$$

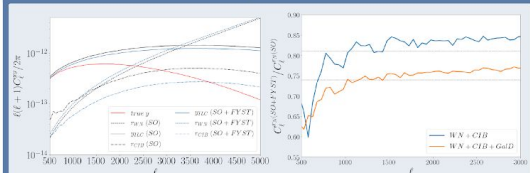
T our maps at a frequency i , a_i the intensity change of the component of interest s and n_i the Astrophysical contaminants + instrumental noise at each frequency.

$$\sum_i \omega_i a_i = 1 + Var(s) \text{ minimum} \Rightarrow \vec{\omega} = \frac{R^{-1} \vec{a}}{\vec{a}^T R^{-1} \vec{a}} \quad (3)$$

Where R is the covariance matrix of the data. We define the residual noise as :

$$r_N = \sum_i \omega_i n_i(p) = s_{ILC} - \sum_i \omega_i a_i s(p) \quad (4)$$

Early results



We find that cumulative CIB+Instrumental ILC residual noise is reduced by 18% when combining SO and FYST rather than for SO alone. When adding galactic dust to the sky, this rises to 26%.

Next steps

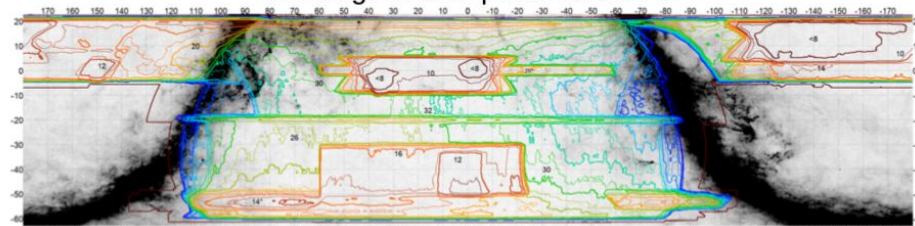
- Make the mock sky more realistic by including other components of the microwave sky. Add a mask that better fits the survey strategies.
- Separate CIB residual and instrumental noise residual.
- Improve the component separation method, for example, use CILC and quantify the noise penalty.
- Address and quantify CIB bias.

DEMO

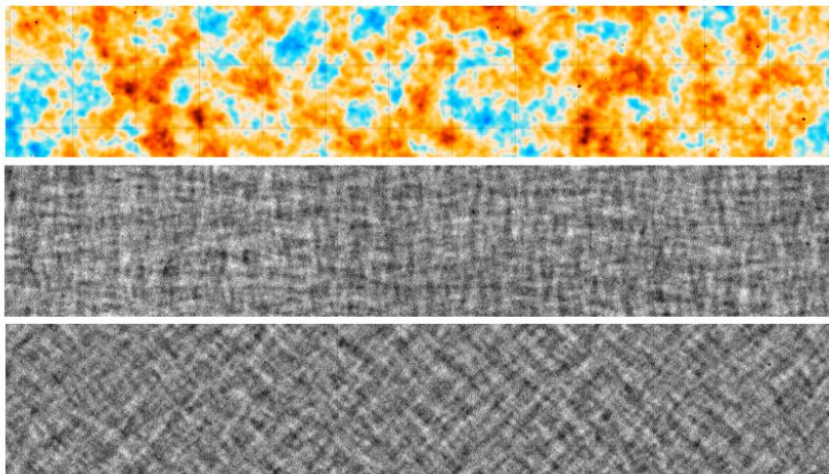
ACT DR5 maps

- 6x as much data as ACT DR4
- 98 GHz, 150 GHz and 220 GHz
- Combined mean depth: 13 $\mu\text{K arcmin}$
- 1.4 arcmin resolution at 150 GHz
- Interim data release not for precision cosmology.
Example usage: point sources, tSZ, kSZ, galactic science, etc.
- Available on LAMBDA now
- Interactive web atlas

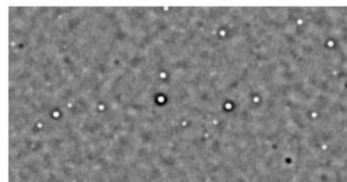
Coverage and depth at 150 GHz



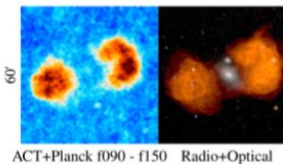
ACT+Planck CMB intensity and polarization



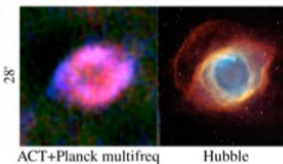
Point sources & clusters



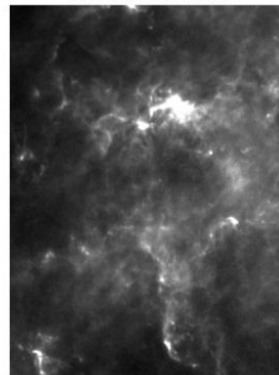
Fornax A



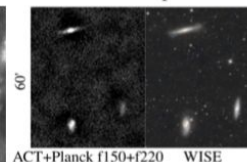
Helix Nebula



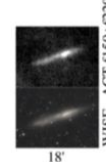
Galactic dust



Leo Triplet



NGC 55



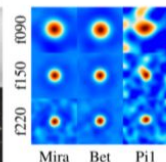
NGC 253



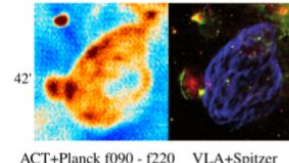
Merging clusters



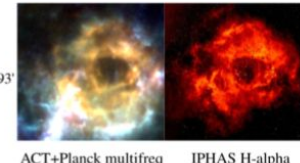
Stars



Supernova remnant W44



Rosette nebula





Maya Mallaby-Kay

Graduate Student
Advisor: Jeff McMahon
University of Chicago

&

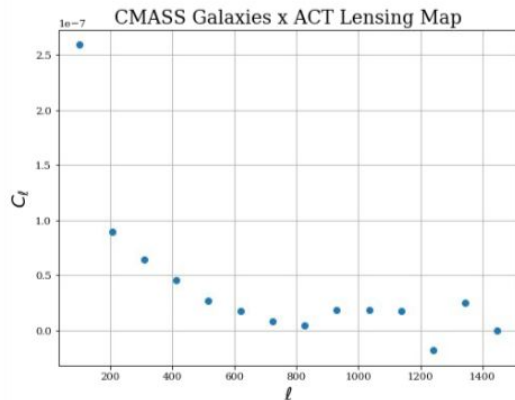
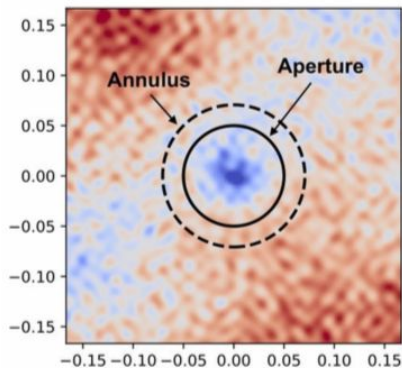
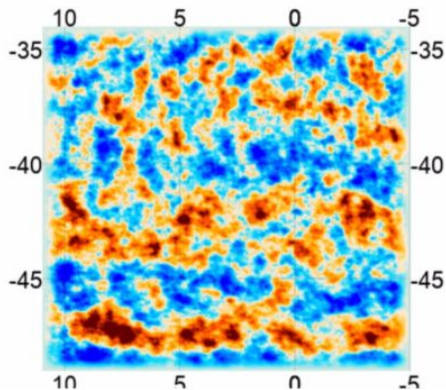
Zach Atkins

Graduate Student
Advisor: Jo Dunkley
Princeton University



ACT DR4 & DR5 IPython Notebooks

- 12 IPython notebooks
- Provide simple analysis examples that reflect some of the plots presented in the DR4/5 papers
- Demonstrate how to use the DR4 & DR5 data products



ACT DR5 Demos
March 11 at 2:15,
2:50 and 3:25 pm
PT!

Notebooks
Available through
LAMBDA

Viewing and Apodizing Maps Studying DR5 Clusters

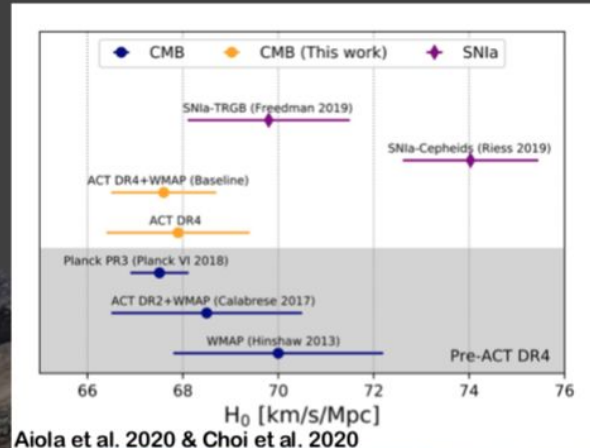
Quick Lensing x CMASS
Galaxies example

[arXiv:2103.03154](https://arxiv.org/abs/2103.03154)

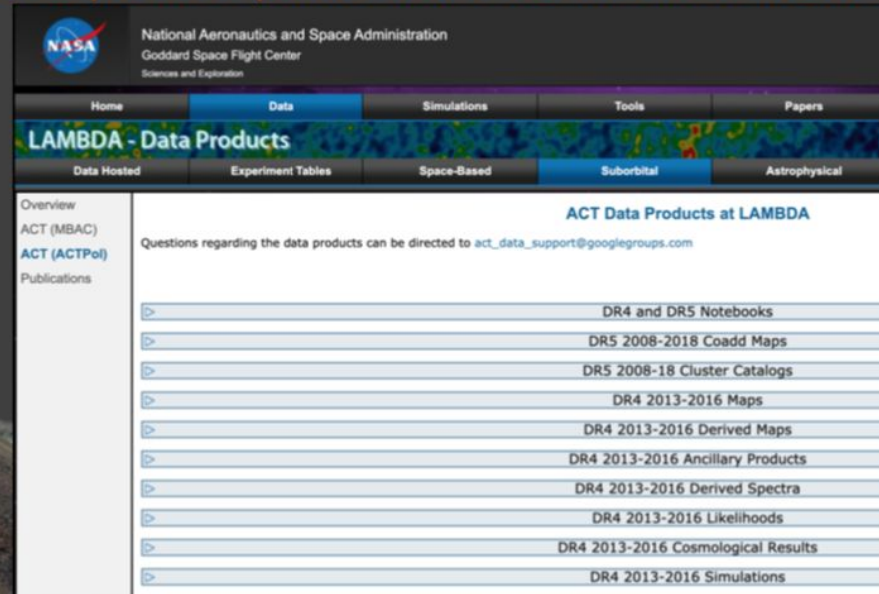
ACT Demos:

- ACT DR4 and DR5 Public Data Products (myself)
- ACT DR5 Maps “Meet-and-Greet” (Sigurd N.)
- ACT DR4 and DR5 Notebooks (Maya M-K. & Zach A.)

When: Thursday March 11 @ 2:15, 2:50, 3:25pm PT



Data products public on NASA LAMBDA and NERSC



National Aeronautics and Space Administration
Goddard Space Flight Center
Sciences and Exploration

Home Data Simulations Tools Papers

LAMBDA - Data Products

Data Hosted Experiment Tables Space-Based Suborbital Astrophysical

Overview
ACT (MBAC)
ACT (ACTPol)
Publications

ACT Data Products at LAMBDA

Questions regarding the data products can be directed to act_data_support@googlegroups.com

- > DR4 and DR5 Notebooks
- > DR5 2008-2018 Coadd Maps
- > DR5 2008-18 Cluster Catalogs
- > DR4 2013-2016 Maps
- > DR4 2013-2016 Derived Maps
- > DR4 2013-2016 Ancillary Products
- > DR4 2013-2016 Derived Spectra
- > DR4 2013-2016 Likelihoods
- > DR4 2013-2016 Cosmological Results
- > DR4 2013-2016 Simulations

CMB-S4 Online Services - Julian Borrill

The new range of CMB-S4 online services includes:

- The website, including the private team area
- The membership database
- The mailing lists
- The Google drive
- The Confluence collaboration & project space wikis
- The DocDB document archive
- The Indico conference site
- The Slack workspace
- The GitHub organization

Come for a 15-minute tour at 3pm Pacific

Followed by Q&A/individual troubleshooting